Al/Ga-doped $Li_7La_3Zr_2O_{12}$ Garnets as Li-ion solid-state battery electrolytes

Karasulu, Bora; Emge, Steffen P.; Groh, Matthias F.; Grey, Clare P.; Morris, Andrew J.

DOI:
10.1021/jacs.9b12685

Document Version
Publisher's PDF, also known as Version of record

Citation for published version (Harvard):
Karasulu, B, Emge, SP, Groh, MF, Grey, CP & Morris, AJ 2020, 'Al/Ga-doped $Li_7La_3Zr_2O_{12}$ Garnets as Li-ion solid-state battery electrolytes: atomistic insights into local coordination environments and their influence on ^{17}O, ^{27}Al, and ^{71}Ga NMR spectra', *Journal of the American Chemical Society*, vol. 142, no. 6, pp. 3132-3148. https://doi.org/10.1021/jacs.9b12685

JACS
JOURNAL OF THE AMERICAN CHEMICAL SOCIETY

pubs.acs.org/JACS

Article

Al/Ga-Doped $Li_7La_3Zr_2O_{12}$ Garnets as Li-Ion Solid-State Battery Electrolytes: Atomistic Insights into Local Coordination Environments and Their Influence on ^{17}O, ^{27}Al, and ^{71}Ga NMR Spectra

Bora Karasulu,[‖] Steffen P. Emge,[‖] Matthias F. Groh, Clare P. Grey,* and Andrew J. Morris*

Cite This: *J. Am. Chem. Soc.* 2020, 142, 3132−3148

Read Online

ACCESS | Metrics & More | Article Recommendations | Supporting Information

ABSTRACT: $Li_7La_3Zr_2O_{12}$ (LLZO) garnets are among the most promising solid electrolytes for next-generation all-solid-state Li-ion battery applications due to their high stabilities and ionic conductivities. To help determine the influence of different supervalent dopants on the crystal structure and site preferences, we combine solid-state ^{17}O, ^{27}Al, and ^{71}Ga magic angle spinning (MAS) NMR spectroscopy and density-functional theory (DFT) calculations. DFT-based defect configuration analysis for the undoped and Al and/or Ga-doped LLZO variants uncovers an interplay between the local network of atoms and the observed NMR signals. Specifically, the two characteristic features observed in both ^{27}Al and ^{71}Ga NMR spectra result from both the deviations in the polyhedral coordination/site-symmetry within the 4-fold coordinated Li1/24d sites (rather than the doping of the other Li2/96h or La sites) and with the number of occupied adjacent Li2 sites that share oxygen atoms with these dopant sites. The sharp ^{27}Al and ^{71}Ga resonances arise from dopants located at a highly symmetric tetrahedral 24d site with four corner-sharing LiO_4 neighbors, whereas the broader features originate from highly distorted dopant sites with fewer or no immediate LiO_4 neighbors. A correlation between the size of the $^{27}Al/^{71}Ga$ quadrupolar coupling and the distortion of the doping sites (viz. $XO_4/XO_5/XO_6$ with X = {Al/Ga}) is established. ^{17}O MAS NMR spectra for these systems provide insights into the oxygen connectivity network: ^{17}O signals originating from the dopant-coordinating oxygens are resolved and used for further characterization of the microenvironments at the dopant and other sites.

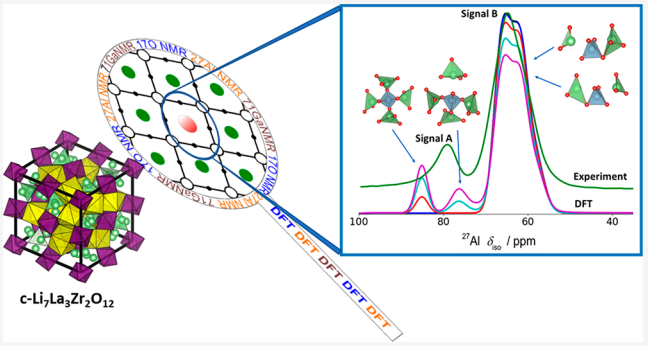

1. INTRODUCTION

Li-stuffed garnets have received widespread attention as solid electrolytes for next-generation Li-ion batteries and have been studied extensively since the discovery of $Li_7La_3Zr_2O_{12}$ (LLZO).[1] The cubic variant of LLZO garnet features high Li-ion conductivity (σ_{Li} = 10^{-3} to 10^{-4} S/cm at ambient temperature), accompanied by a near-unity Li-ion transference number.[1−3] In addition to its thermal and mechanical robustness, LLZO also displays superior electrochemical stability against Li-metal rendering LLZO an ideal solid electrolyte for Li-metal-based batteries.[2,4]

Two polymorphs of LLZO have been reported, a tetragonal ($I4_1/acd$, SG no. 142)[5−8] low-temperature form and a cubic ($Ia\bar{3}d$, SG no. 230)[3,7,9−11] polymorph that is thermodynamically stable above 400−625 K (the exact value depending on the sample impurity level).[1,3,12] However, doping by supervalent cations (Al^{3+}, Ga^{3+}, Ta^{5+}, etc.) enables the stabilization of the cubic form at room temperature.[3,13,14] Of these, Al doping is the most common, since samples are generally prepared by sintering at high temperatures (T > 1470 K) using an Al_2O_3 crucible (Al doping thus arising from Al-contamination).[1,3,5,8,12,14]

The low-temperature tetragonal phase is fully ordered comprising full occupancy (site-occupancy factor, g = 1) of the three lithium sites, namely, the tetrahedral Li1/T(8a), and the octahedral Li2/O(16f) and Li3/O(32g) sites. Cubic LLZO features two Li site groups: the tetrahedral Li1/24d and the octahedral Li2/[48g/96h] (Figure 1). The Li2 site is a split position with the two 96h sites separated by 0.77 Å, and the 48g site sitting in the center. This site group cannot be fully occupied, resulting in a partial occupancy, contributing to the Li mobility.[3,7,9−11,15]

Received: November 25, 2019
Published: January 17, 2020

https://dx.doi.org/10.1021/jacs.9b12685
J. Am. Chem. Soc. 2020, 142, 3132−3148

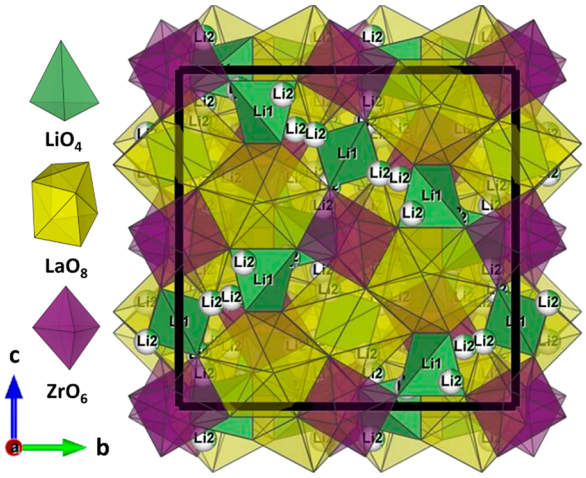

Figure 1. Representation of the individual crystallographic sites in the crystal structure of cubic-$Li_7La_3Zr_2O_{12}$ (c-LLZO, $Ia\bar{3}d$). The Li1, La, and Zr atoms reside inside a green, yellow, and purple coordination polyhedral, respectively, and the O atoms are located at the vertices. Li2/96h split positions are shown by green−white balls. The unit cell is depicted with a thick, solid black line. The close spatial proximity (0.77 Å) between the Li2 sites is clearly seen.

The local structure of doped c-LLZO has been the subject of several studies in recent years to understand both the mechanism of the unusually high lithium-ion conductivity and the influence of different dopants. Solid-state NMR spectroscopy as a local structural probe has been the technique of choice in many studies, since the observed chemical shifts are determined by the local environment of the nuclei.[16] For example, typical ^{27}Al chemical shift ranges are 70−90 ppm for AlO_4, 25−40 ppm for AlO_5, and −10 to 15 ppm for AlO_6 environments.[17] However, due to a large divergence in experimental and theoretical results the influence of the dopants is still not well understood.

Solid-state ^{27}Al-NMR spectra of Al-doped c-LLZO always feature one signal at around 64−68 ppm.[3,18−24] In addition, several research groups have reported an additional signal around 78−82 ppm.[3,18,19,23] One of these signals is usually assigned to a tetrahedral AlO_4 environment, created by substituting Li1 sites in the garnet structure. However, both signals reside in the shift range usually assigned to AlO_4 environments. Since the cubic structure model (Figure 1) contains only one possible tetrahedral crystallographically distinct environment (i.e., the original Li1 site), the nature of the second environment is still a subject of discussion.[25] Suggested possibilities include Al substitution on the La, or Zr sublattices, or on the second Li site where it could adopt a pseudotetrahedral/octahedral local coordination geometry.[22,23,26−28]

Ga-doped c-LLZO has a similar story: in the ^{71}Ga-NMR spectra, a broad feature due to a species with a large quadrupolar coupling constant, C_Q (>10 MHz) is always present.[22,23,26−28] However, an additional relatively sharp signal arising from a much smaller C_Q (<5 MHz) has also been reported in a few studies.[22,27,28] Again, both of these signals are in the shift region usually expected for tetrahedral Ga-environments, providing only limited information on the actual coordination environments.

Like ^{27}Al, the $^{69/71}$Ga chemical shifts are strongly dependent on their local environment. Usually, 4-fold coordinated Ga resonances are found between 107 and 222 ppm, while 6-fold coordination leads to a shift range of −80 to −42 ppm.[17] The most noticeable difference between Al and Ga NMR spectroscopy is the larger quadrupolar moments of $^{69/71}$Ga leading to the much larger second-order quadrupolar (SOQ) broadening, particularly for ^{69}Ga. While comparatively better resolved spectra can be obtained by studying ^{71}Ga, it is generally necessary to go to higher magnetic fields, and fewer $^{69/71}$Ga NMR analyses of LLZO have been reported[22,23,26−28] compared to those for ^{27}Al NMR.[3,18−24]

To probe the connection between the different dopant sites and the observed characteristic NMR features, *ab initio* calculations of solid-state NMR spectral parameters have proven to be an effective tool.[16,29−34] However, the use of density-functional theory (DFT) for understanding the NMR resonances in cubic LLZO garnets has been very limited. To our knowledge, only Rettenwander et al.[24] have presented a DFT-NMR study for cubic LLZO garnets based on an Al^{3+}-dopant configuration analysis, the other DFT studies mainly addressing the structural properties, phase transition, and stability of c-LLZO and Li^+ diffusion therein.[6,7,13,35−46] To date, no DFT study has addressed the ^{71}Ga or ^{17}O NMR spectra of c-LLZO.

Using DFT, Rettenwander et al. proposed that ^{27}Al NMR signals originate from Al^{3+} ions with slightly different (and only) 4-fold coordination at the crystallographic Li1/24d and Li2/96h sites in cubic LLZO garnet.[24] However, their predicted NMR parameters (with C_Q = 0.8−3.3 MHz) do not cover the whole range of experimentally observed parameters (with C_Qs ranging from 3.3 to 6.9 MHz). In other words, the broad features observed in the experiments (stemming from the higher C_Qs) may not be adequately explained by the AlO_4/AlO_5/AlO_6 sites considered in their simulation models. Moreover, the effect of varying the dopant concentrations in the lattice on the corresponding NMR shifts and C_Q values was not considered.

Given the ambiguities in the literature, a more comprehensive sampling of the dopant sites is needed to unravel the distinct local interaction networks and to determine which crystallographic sites and local environments the observed NMR signals originate from. In this study, we therefore present the ^{27}Al, ^{71}Ga, and ^{17}O magic angle spinning (MAS) spectra of Al- and Ga-doped cubic LLZO along with a comprehensive and systematic first-principles defect-configuration analysis for these c-LLZO variants. Based on our quantum-mechanical (DFT/GIPAW-NMR) calculations, we assign all NMR signals to specific local structure features and show that the dopants only reside on the Li1/24d sites (with varying local distortions). The ^{17}O MAS spectra, presented here for the first time for the LLZO system, show distinct and well-resolved resonances that are due to oxygen bound to the dopants (Al or Ga). These atomistic insights will benefit the devising of strategies to optimize ionic conductivity in doped LLZO variants. The presented general trends will also contribute to the understanding of similar local environments in other related energy materials.

2. METHODS

2.1. Computational Details. Plane-wave DFT electronic structure calculations were performed using the CASTEP code[47,48] (v. 17.21), which is an implementation of periodic boundary conditions within the pseudopotential approximation. The generalized-gradient approximation (GGA) was used of the Perdew−Burke−Ernzerhof (PBE) exchange-correlation functional form.[49] The Brillouin zone was sampled using a Monkhorst−Pack (MP) grid[50] with a *k*-point spacing

https://dx.doi.org/10.1021/jacs.9b12685
J. Am. Chem. Soc. 2020, 142, 3132−3148

finer than $2\pi \times 0.05$ Å^{-1}. Plane-wave basis sets were truncated at a cutoff energy of 800 eV, and a convergence criterion of 2×10^{-8} eV/atom was used in the self-consistent optimization of the electronic wave function. The atomic positions and lattice parameters were fully relaxed at this level of accuracy using LBFGS optimizer[51,52] until all forces were smaller than 0.05 eV/Å. All *ab initio* calculations employ the ultrasoft pseudopotentials generated by the CASTEP on-the-fly generator (v.17, the corresponding strings are given in the SI, Part 2B).

Solid-state ^{17}O, ^{27}Al, and ^{71}Ga NMR chemical shifts were computed using *ab initio* methods for a selection of pristine and doped LLZO variants. The magnetic response calculations were carried out by applying the gauge-including projector augmented wave (GIPAW) approach.[53,54] By fitting the computed isotropic shielding data against the experimental chemical shifts (as detailed in the SI, Part 3), we obtained σ_{ref} values of 242.1, 556.5, and 1674.5 ppm for ^{17}O, ^{27}Al, and ^{71}Ga NMR shifts, respectively. These σ_{ref} values have facilitated the accurate assignment of the experimental peaks to the computed ones.

Quadrupolar properties were calculated using the GIPAW method utilizing the electric field gradient (EFG) that is derived directly from the lattice structure and final electron density distribution.[55] GIPAW yields the quadrupolar constant (C_Q) and the asymmetry parameter (η_Q), which are used jointly with the δ_{iso} values to construct the final MAS NMR spectra with SOPRANO,[56] including the first- and second-order quadrupolar effects (e.g., shifts and broadening). Corresponding to a 16.44 T magnetic field strength, the Larmor frequencies of 94.95 MHz for ^{17}O, 213.5 MHz for ^{71}Ga, and 182.58 MHz for ^{27}Al were used in all simulations of NMR spectra using the parameters extracted from the DFT calculations. Higher-accuracy DFT settings were adopted for NMR calculations (as detailed in the SI, Part 2).

The thermodynamic phase stability of different phases of LLZO was assessed by comparing their free energies with those of the competing species/compounds. We define the formation energy per atom (E_f/atom) of a compound $X_aLi_bLa_cZr_dO_e$, where the dopant X = {Al, Ga}, as

$$\frac{E_f}{\text{atom}} = \frac{E\{X_aLi_bLa_cZr_dO_e\} - a\mu_X - b\mu_{Li} - c\mu_{La} - d\mu_{Zr} - e\mu_O}{a + b + c + d + e} \quad (1)$$

where $E\{X_aLi_bLa_cZr_dO_e\}$ is the total DFT energy of a given structure, $X_aLi_bLa_cZr_dO_e$, and $\mu_{\{X,Li,La,Zr,O\}}$ are the chemical potentials of the constituent atomic species (where usually $c = 3$, $d = 2$, and $e = 12$). This relation is valid under the assumption that the Gibbs energy can be approximated by the internal energy, since the pV and thermal energy contributions are negligible at 0 K.

The elemental contributions (i.e., chemical potentials) can be determined from (a) their individual ground-state elemental structure, e.g., Li in the *P*63/*mmc* space group, or from (b) their contributions in the starting (reference) materials, used to synthesize the pristine/doped LLZO, e.g., Li_2O, La_2O_3, ZrO_2, Ga_2O_3, and/or Al_2O_3. For the latter option, one needs to solve the linear equations relating the DFT total energies with chemical potentials of contributing atoms (i.e., $\mu_{\{X,Li,La,Zr,O\}}$ to be used in eq 1). This is exemplified in the SI, Part 2B. The choice of the reference materials may be relevant not only in the quantitative comparison of the relative stabilities of LLZO variants but also in their qualitative order (see Section 3.2.1 and the SI, Part 5).

For the detailed analysis of the distortion within the polyhedral coordination of the dopant sites, the following methods were adopted, as described in their original references without any modifications: effective coordination number,[57] distortion index (DI),[58] quadratic elongation (QE),[59] and bond-angle-variance.[59,60] Bond valence sums (BVSs) were also used, adopting the empirical constant, $B_0 = 0.37$ Å, and bond valence parameters (l_0) taken from refs 61 and 62.

Following from Baur et al.,[58] the distortion index (DI) is defined as

$$\text{DI} = \frac{1}{n}\sum_{i=1}^{n}\left(\frac{|X_i - X_{avg}|}{X_{avg}}\right) \quad (2)$$

where X corresponds to the different parameters, viz. bond length, bond angle, or polyhedral edge. In addition, X_i is the value of a given parameter for the coordinating ith atom with respect to the central atom within a particular polyhedron, whereas X_{avg} is the average for a given parameter.

Images of the crystal structures were prepared using VESTA,[63] while the data plots were generated using ORIGIN v9.1.

2.2. Experimental Details. *2.2.1. Synthesis.* Gram-scale batches (e.g., 1.6 g) of Al and Al + Ga substituted LLZO ($Li_{7-(3x-y)}Ga_xAl_yLZO$, Al_yGa_x-LLZO) were synthesized by following a modified literature procedure.[64] Li_2CO_3 (99.997%, Aldrich, including 10 wt % excess), La_2O_3 (Alfa-Aesar, 99.999%), ZrO_2 (Alfa-Aesar, 99%, calcined), Al_2O_3 (Aldrich, p.a. nanopowder <50 nm), and Ga_2O_3 (Alfa-Aesar, 99.999% metal basis) were mixed according to the stoichiometric ratio of LLZO and ball-milled for 2 × 20 min with a Mixer/Mill 8000 M instrument (*SPEX* SamplePrep) using a zirconia jar with two zirconia balls ($d = 10$ mm). The powdered samples were placed in alumina crucibles and calcined in O_2 flow at 1000 °C for 12 h in a tube furnace after heating with a rate of 5 K/min, followed by natural cooling. Afterward, the samples were reground and calcined again in O_2 flow under the same conditions. After the synthesis, samples were immediately transferred into an Ar-filled glovebox (*VAC* or *MBraun* ($p(O_2)/p^0 \leq 1$ ppm, $p(H_2O)/p^0 \leq 1$ ppm).

2.2.2. ^{17}O Enrichment Procedure. Enriched LLZO was obtained by heating the as-synthesized powder (ca. 0.4 g) to 550 °C under an atmosphere of 70% enriched $^{17}O_2$ (Cambridge Isotope Laboratories, used as received) in a closed quartz tube for days.

2.2.3. Solid-State MAS NMR. ^{71}Ga, ^{27}Al, and ^{17}O NMR spectra were acquired on Bruker 700 MHz (16.4 T) and 500 MHz (11.8 T) magnets with Avance III consoles using Bruker 1.3 mm HXY (16.4 and 11.8 T magnets) and 2.5 mm HFX MAS probes (11.8 T magnet) by using regular zg/one-pulse pulse programs with a small flip angle ($\ll\pi/2$, i.e., $<\pi/4$ for ^{71}Ga and $<\pi/6$ for ^{27}Al and ^{17}O). The spectra were externally referenced against CeO_2 powder (878 ppm)[65,66] or H_2O (0 ppm) for ^{17}O, $Ga_2(SO_4)_3$ powder (low C_Q signal, −87 ppm)[67] for ^{71}Ga, and AlF_3 powder (−17 ppm)[68] for ^{27}Al. The latter compounds were used for pulse length optimization as well.

All samples were ground in agate mortars and packed into 1.3 mm or 2.5 mm ZrO_2 rotors under an argon atmosphere inside a glovebox (M. Braun; $p(O_2)/p^0 < 1$ ppm, $p(H_2O)/p^0 < 1$ ppm). The MAS NMR experiments were performed at sample spinning speeds of 45 and 50 kHz (1.3 mm) or 25 kHz (2.5 mm).

Two-dimensional ^{27}Al 3QMAS (triple quantum MAS) NMR spectra were acquired on Bruker 700 MHz (16.4 T) and 200 MHz (4.70 T) magnets with Avance III consoles using Bruker 1.3 mm HXY (16.4 T magnet, MAS = 50 kHz) and 4.0 mm HX MAS probes (4.70 T magnet, MAS = 10 kHz). For further details refer to the Supporting Information (SI).

Bruker Topspin 3.5 pl7 was used for raw data handling and processing.[69] The ^{71}Ga and ^{27}Al spectra were fitted with DMFIT software[70] to obtain values of C_Q and η_Q using the *Q-MAS 1/2* model to fit the central transition assuming infinitely fast MAS.

3. RESULTS

3.1. Experimental NMR Results. *3.1.1. Medium and High Field ^{27}Al MAS NMR.* Figure 2 shows ^{27}Al MAS NMR spectra of different Al-containing LLZO compounds at two different magnetic field strengths, 11.8 T (a) and 16.4 T (b). In all cases but one, we observed two components in the chemical shift range of approximately 40−90 ppm, henceforth labeled as A for the usually sharper component with a higher shift and B for the broader component with a lower shift. In the case of $Ga_{0.3}Al_{0.1}$LLZO no component A was observed in the 11.8 T field, but considering the low intensity of this component for the same compound in the higher field measurement, it was most likely too low in intensity in this case to be detected above the noise.

While component B lies in the lower shift range typically found for AlO_4 tetrahedra, its shift is consistent with shifts seen for tetrahedral sites in, for example, some Al_2O_3 structures.[17]

https://dx.doi.org/10.1021/jacs.9b12685
J. Am. Chem. Soc. 2020, 142, 3132−3148

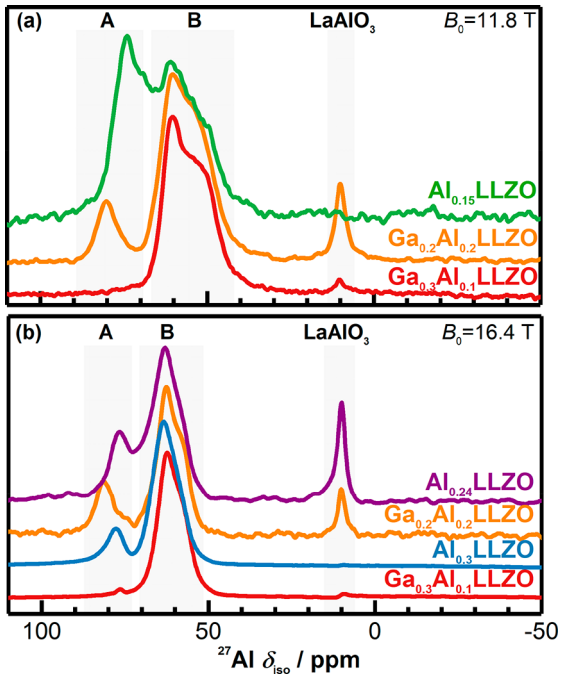

Figure 2. ^{27}Al MAS NMR of LLZO samples in (a) 11.8 T field (MAS = 25 kHz, except 30 kHz for $Ga_{0.3}Al_{0.1}$LLZO) and (b) 16.4 T field (MAS = 50 kHz, except 40 kHz for $Ga_{0.2}Al_{0.2}$LLZO). The observed components are labeled A–B from higher to lower shifts. ^{27}Al MQMAS spectra are shown in Figure S1.

The broad and asymmetric (second-order quadrupolar, SOQ) peak shape, and the decrease in peak width at higher fields (compare Figure 2a,b), is consistent with a large C_Q as confirmed by previous studies[3,23,24]

Component A lies in the higher shift range of tetrahedral Al-environments, with a shift that is more common for Al halides.[71] A few noticeable exceptions occur; e.g., the AlO_4 environments in $Y_4Al_2O_9$ and $CaAl_2O_4$ resonate at 78.2 and 76.2 ppm[72] as well as 69.5–86.2 ppm,[73] respectively, the O atoms of the AlO_4 polyhedra also being coordinated to large cations with high ionicity. The signal at approximately 10 ppm is usually associated with the $LaAlO_3$ impurity commonly observed in these samples.[23]

To help obtain a set of reliable quadrupolar parameters,^{27}Al MQMAS NMR spectra of $Al_{0.24}$LLZO were acquired at 16.4 T. This composition was chosen specifically for its high Al-content while still being below the different suspected solubility limits of Al^{3+} in LLZO, specifically $Al_{0.25}$[74] and $Al_{0.53}$[10,28,43,75] depending on the study, thus maximizing the signal-to-noise ratio while reducing the risk of impurity signals. Our MQMAS results indicate that two signals with slightly different isotropic shifts (66 vs 68 ppm) contribute to the broad signal B (see Figure S1). This is in contrast to previous studies[3,23] where only one signal for B was resolved, albeit with broadening consistent with both a distribution of chemical shifts and C_Q values, indicating a distribution of environments and the presence of more than one site.[3] These differences are ascribed to variations between samples and the use of the lower field and higher spinning speed used here, which will lead to a larger separation and better resolution of sites with different C_Qs. The parameters extracted from the fit are summarized in Table 1, signal B having a higher C_Q (5.5 and 6.3 MHz) than signal A (3.5 MHz), suggesting a less symmetric environment. Figure S1 shows the fitting of the 1D slices of the ^{27}Al spectrum MQMAS of $Al_{0.24}$LLZO as well as the overlapping experimental and simulated ^{27}Al MQMAS spectra.

3.1.2. High Field ^{71}Ga MAS NMR. Figure 3 shows the ^{71}Ga MAS NMR spectra of $Ga_{0.3}Al_{0.1}$LLZO (a) and $Ga_{0.2}Al_{0.2}$LLZO

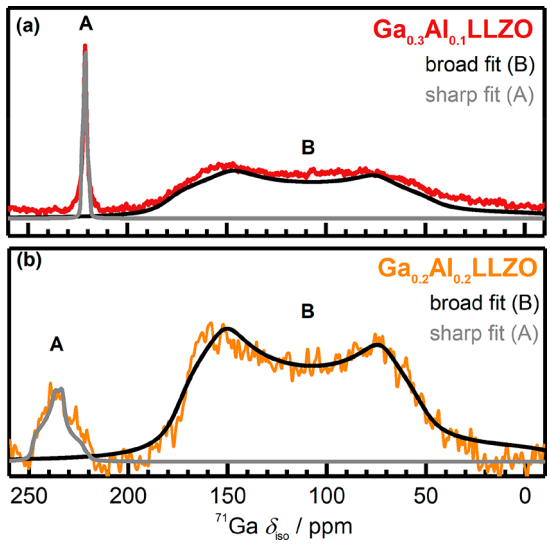

Figure 3. ^{71}Ga-NMR acquired at 16.4 T for (a) $Ga_{0.3}Al_{0.1}$LLZO (red) MAS = 50 kHz, and (b) $Ga_{0.2}Al_{0.2}$LLZO (orange) MAS = 40 kHz; together with the fitted spectra (broader component B in black and component A in gray). Fit parameters used are summarized in Table 1.

(b) acquired at 16.4 T. The ^{71}Ga spectra are similar to the ^{27}Al spectra showing two components, one comparatively sharp signal (A), now with an apparent shift of about 230 ppm, and a broad signal (B) ranging 50–200 ppm, suggesting 4-fold ^{71}Ga coordination.[17] Due to the similarities of Ga and Al shift behavior and the fact that they often appear in similar compounds, empirical formulas describing the linear relationship between Al and Ga shifts have been derived in the past.[76,77] Using the ^{27}Al shifts as a starting point, one can calculate ^{71}Ga

Table 1. ^{27}Al and ^{71}Ga Parameters Obtained from the Fits of Various Al- and Ga-Containing LLZO Samples Shown in Figures 2 (SI, Figure S1) and 3

type	LLZO variant	fitted component	δ_{iso} [ppm]	C_Q [MHz]	η_Q
^{27}Al	$Al_{0.24}$	Al1 (sharp signal A)	80 ± 0.5	3.5 ± 0.3	0.6 ± 0.1
	$Al_{0.24}$	Al2 (broad signal B)	68 ± 0.5	6.2 ± 0.3	0.3 ± 0.1
	$Al_{0.24}$	Al3 (B)	66 ± 0.5	5.5 ± 0.3	0.5 ± 0.2
^{71}Ga	$Ga_{0.3}Al_{0.1}$	Ga1 (A)	223 ± 5	1.8 ± 0.5	0.7 ± 0.2
	$Ga_{0.3}Al_{0.1}$	Ga2 (B)	196 ± 5	12 ± 0.5	0.3 ± 0.1
	$Ga_{0.2}Al_{0.2}$	Ga1 (A)	249 ± 5	4.4 ± 0.5	0.7 ± 0.2
	$Ga_{0.2}Al_{0.2}$	Ga2 (B)	193 ± 5	12 ± 0.5	0.2 ± 0.1

https://dx.doi.org/10.1021/jacs.9b12685
J. Am. Chem. Soc. 2020, 142, 3132–3148

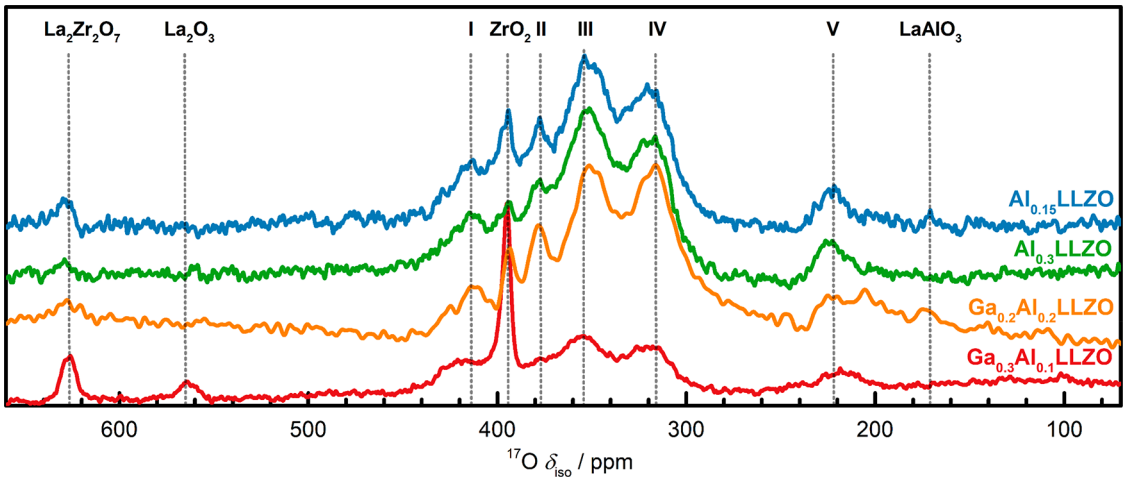

Figure 4. ^{17}O NMR of $Ga_{0.3}Al_{0.1}$LLZO, $Al_{0.3}$LLZO, $Al_{0.15}$LLZO (all 16.4 T), and $Ga_{0.2}Al_{0.2}$LLZO (11.8 T). The observed components assigned to LLZO are labeled I−V from higher to lower shifts, while impurity signals are assigned to their most likely origin (e.g., ZrO_2 which is used as the NMR rotor, i.e., the sample container).

shifts that are nearly identical to those observed in the experiments (see eq S1 and Table S3), supporting the proposal that Al and Ga dopants are found in similar environments in the LLZO structure.

The fits of the ^{71}Ga NMR spectra used to extract the δ_{iso}, C_Q, and η_Q values are summarized in Table 1. The broad peak B shows a large C_Q of 12 MHz and an η_Q of 0.2−0.3, while the sharp peak A shows a much smaller C_Q of 2−4 MHz. This suggests either a more symmetric local environment or dynamical averaging of the second-order quadrupolar interaction for component A. Due to the featureless line shape of A, no reliable η_Q value could be determined, and the fitting parameters for both A and B have a considerably wide margin of error, in particular η_Q. Figure S2 illustrates that a good fit, e.g., for the broad component, can be achieved for a range of values for η_Q, without a large influence on the extracted values of C_Q and δ_{iso} (Table S2): while we picked η_Q = 0.3 as the best fit for the broad signal from $Ga_{0.3}Al_{0.1}$LLZO, values from 0.2 up to 0.4 also gave a reasonably good fit. (We applied the minimal line broadening necessary to get a good fit while retaining the spectral features.) As observed for the ^{27}Al MQMAS data, it is likely that multiple local environments contribute to signal B.

3.1.3. ^{17}O NMR MAS NMR. ^{17}O NMR is a complementary technique to ^{27}Al and ^{71}Ga NMR as it allows the effect of the dopants on the local environments in the lattice to be probed. Since oxygen is distributed over the whole structure, a more complete picture of the local environments can be obtained. ^{17}O enrichment of the materials is aided in these materials by the acceptable oxygen mobility previously observed,[78] allowing a lower than commonly used[79,80] enrichment temperature of a ceramic of only 550 °C. Our intention was to keep the Li loss at elevated temperatures to a minimum.

The ^{17}O MAS NMR spectra of the differently doped LLZO compounds show a multitude of signals with only small differences being observed depending on the dopant level (Figure 4). This suggests a limited influence of the doping on the overall lattice structure. The ^{17}O spectrum of $Ga_{0.2}Al_{0.2}$LLZO was acquired at a lower field strength than all the others, yet similar shifts are observed, indicating that the oxygen environments are associated with low C_Q values (Figure S3).

Overall, up to nine signals are visible, five of which can be assigned to the expected impurities. The background signal from the ZrO_2 rotor used as sample container is observed at approximately 380 ppm. Common impurities are $La_2Zr_2O_7$ (with a reported peak at 623 ppm and an even more intense peak that overlaps with the ZrO_2 signal),[81] La_2O_3 (584 ppm),[65,82] and $LaAlO_3$ (^{17}O ppm),[83] which is also visible in the ^{27}Al-NMR spectra. This leaves signals I (413 ppm), II (378 ppm), III (352 ppm), IV (317 ppm), and V (225 ppm) as signals originating from the LLZO oxygen atoms. Although the shifts are clearly in the shift range seen for other zirconates,[84,85] assignments are impossible without the use of DFT calculations.

3.2. Computational Results. In order to provide an atomic-level understanding of the source of the ^{17}O, ^{27}Al, and ^{71}Ga NMR peaks, we have performed extensive DFT-GIPAW NMR calculations on the undoped and Al/Ga-doped cubic LLZO variants. Numerous defect configurations were first generated by employing a DFT-based sequential enumeration approach. To obtain the initial representative structure for the pristine cubic LLZO phase (c-$Li_7La_3Zr_2O_{12}$), we started from the fully lithiated model (c-$Li_{15}La_3Zr_2O_{12}$) and introduced Li vacancies on the Li2 site in a systematic stepwise approach to achieve the final composition (see the Supporting Information, Part 2A, for details). We then introduced varying levels of Al and Ga dopants on the La, Li1, and/or Li2 sites removing the two nearest 2 Li ions (per dopant) to attain charge neutrality (only for Li substitutions), using a similar enumeration approach to create defect configurations. To limit the computational efforts, the smaller primitive unit cell of c-$Li_7La_3Zr_2O_{12}$ (Z = 4, 96 atoms, $R\bar{3}c$, SG = 167) was used in the DFT calculations.

3.2.1. Thermodynamic Phase Stability of LLZO Variants. The relative stability, using the relaxed structures of the LLZO phases under investigation (i.e., optimized atomic positions and lattice parameters), was derived from the corresponding DFT total energies. Table 2 compiles the defect formation energies (at 0 K) for various undoped and doped LLZO phases, computed using two different reference sets (comprising unary or binary starting materials). The higher stability of the tetragonal phase over the cubic one in the absence of doping (ΔE = ca. 0.01 eV/atom) is noted, in line with previous reports.[1,5,8,42] The cubic phase is stabilized upon doping of the Li1 site (regardless of the dopant type, Al or Ga) becoming as stable as the tetragonal phase, and even more stable in some cases (for all reference sets considered, Tables 2 and Table S5).

https://dx.doi.org/10.1021/jacs.9b12685
J. Am. Chem. Soc. 2020, 142, 3132−3148

Table 2. Formation Energies (E_f/atom, in eV) for Selected $Li_7La_3Zr_2O_{12}$ (LLZO) Variants[a]

compound type	doping site	ref A (unary)	ref B (binary)
tetragonal (t-Li_7LZO)		−2.723	−0.066
cubic (c-Li_7LZO)		−2.714	−0.058
1 Al-doped (c-$Al_{0.25}Li_{6.25}$LZO)	Li1	−2.770	−0.066
	Li2	−1.385	1.319
	La	−2.689	−0.038
1 Ga-doped (c-$Ga_{0.25}Li_{6.25}$LZO)	Li1	−2.740	−0.067
	Li2	−1.516	1.157
	La	−2.664	−0.044
2 Al-doped (c-$Al_{0.5}Li_{5.5}$LZO)	Li1	−2.825	−0.071
2 Ga-doped (c-$Ga_{0.5}Li_{5.5}$LZO)	Li1	−2.765	−0.073
1 Al + 1 Ga (c-$Al_{0.25}Ga_{0.25}Li_{5.5}$LZO)	Li1	−2.795	−0.072
2 Al + 1 Ga (c-$Al_{0.5}Ga_{0.25}Li_{4.75}$LZO)	Li1	−2.847	−0.072
2 Ga + 1 Al (c-$Al_{0.25}Ga_{0.5}Li_{4.75}$LZO)	Li1	−2.816	−0.073
3 Ga + 1 Al (c-$Al_{0.25}Ga_{0.75}Li_{4.0}$LZO)	Li1	−2.843	−0.080

[a]Computed using eq 1, based on the lowest-energy configuration for each stoichiometry. ref A consists of unary starting materials: isolated Li, La, Zr, O_2, Al, and/or Ga. ref B comprises binary starting materials: Li_2O, La_2O_3, ZrO_2, α-Al_2O_3, and/or β-Ga_2O_3. A more negative E_f/atom value corresponds to a more stable compound. An extended version containing several other references and LLZO variants can be found in Table S5.

By contrast, doping the Li2 and La sites leads to further destabilization of the cubic phase. Therefore, our analysis indicates that the doping of the Li1 sites (regardless of the dopant type) is energetically favored over the doping of other sites (Li2 or La), in line with the previous NMR studies and first-principles calculations.[18,20,22,28,41,86,87]

Table 2 shows that the preference for the dopant type (Al vs Ga) depends on the choice of the reference set. Specifically, formation energies computed using reference set A (comprising unary starting materials, isolated Li, La, Zr, O_2, Al/Ga solids) clearly favor Al doping over Ga, whereas the other reference set containing binary compounds does not reveal a clear preference. We also note that the finite-temperature thermodynamics might affect the relative stability of phases, favoring the more disordered phases. This, however, is not expected to alter the conclusions drawn using the zero-temperature energetics (as further discussed in the SI, Part 5).

The formation energy of the cubic phase further decreases (i.e., its stability increases) with increasing doping levels. However, experiments have shown that cubic LLZO is stable only within a certain range of doping levels, namely, $Li_{5.5} < Li_{7-3a} < Li_{6.5-6.8}$ (or $0.07 < a < 0.53$ in $Li_{7-3a}X_aLZO$, widest range known),[10,28,43,75] which corresponds to the substitution of no more than two Al/Ga ions per unit cell ($Z = 4$). Our results suggest that the higher-dopant levels considered here (i.e., those having a Li ratio <5.5) are not unstable with respect to the constituent oxides, or indeed the lower doped materials, but must be unstable with respect to other nongarnet compounds, $LaAlO_3$, and $LiGaO_2$, alongside $La_2Zr_2O_7$, Li_2ZrO_3, $Li_6Zr_2O_7$, and Li_8ZrO_6 (which may also form at low doping levels).[23,28,43,88] This is supported by the defect energies computed vs different decomposition product (see Table S5) which show significant reduction in the stability of the defects, particularly at higher dopant levels. Relevantly, additional ^{27}Al and ^{17}O peaks from nongarnet impurities are often observed particularly at higher doping levels (Figures 2 and 4). While this might also depend on the synthesis procedure, i.e., insufficient mixing and Li excess or loss, it provides a good qualitative explanation of the solubility limit observed experimentally. Ideally, we would use a larger supercell (e.g., $Z = 8$ or larger) to explore more configurations; however, this was not computationally feasible particularly for the full GIPAW-NMR analysis. Despite these concerns, we nonetheless used these higher dopant structures to compute NMR parameters to explore the effect of high dopant concentrations on NMR parameters.

3.2.2. DFT/GIPAW NMR Calculations of Cubic-LLZO Variants. After obtaining the model structures for different levels of Al/Ga doping of LLZO, DFT/GIPAW calculations were performed to obtain the NMR parameters for the ^{17}O, ^{27}Al, and ^{71}Ga isotopes (where applicable). The choice of the density functional, plane-wave cutoff energy, and the MP grid size for k-point sampling was benchmarked, utilizing only the undoped cubic LLZO model (see the SI, Part 4, Figures S11−S13, for details); this benchmark showed that the ^{17}O isotropic shieldings from the GIPAW calculations converged within 0.10 ppm with respect to these criteria. In addition, the choice of exchange-correlation functional (PBE, PBESOL, Rev-PBE, and LDA) does not notably affect the main features in the resulting ^{17}O NMR spectra although some minor features and the overall peak positions (shifts) differ to some extent. We have therefore chosen the PBE functional and the simulation parameters listed in the Computational Details section in order to make the computational efforts tractable.

To compute the NMR spectra, we have included the contributions from all defect configurations that we have considered, by setting their NMR-peak scaling factors either (a) to their Boltzmann weights at selected temperatures (e.g., at 298 K, to capture a realistic combination of low-energy configurations) or (b) to unity, representing an equal contribution from each configuration (to account for the high-energy configurations). We note the relevance of exploring different configurations that are generated by different Li arrangements at 298 K, even though the synthesis was done at higher temperatures (1273 K), because Li atoms are mobile and can still rearrange on cooling the sample from the synthesis temperature. Higher-energy defect configurations may still be accessible and contribute to the final NMR spectrum (at 298 K) given that the samples are cooled rapidly. We simulate this case by considering the higher-temperature distributions (at 1000−4000 K, see below).

While computing the Boltzmann weights, configuration thermodynamics was also taken into account following the formalism outlined by Grau-Crespo et al.[89] We note that even though the choice of reference materials is crucial for computing the formation energies of each individual defect configuration, it does not play a role in determining their Boltzmann weights: the latter relies only on the relative energies with respect to the most-stable configuration for a given stoichiometry.

3.2.2.1. Computed ^{27}Al MAS NMR Spectra. GIPAW/NMR calculations were performed on all 28 defect configurations (i.e., 12 Li1 and 16 Li2 sites for the unit cell with 4 formula units) to determine which Al-dopant sites result in the characteristic NMR resonances. The predicted spectra are presented in Figure 5 where they are compared to the experimental $Al_{0.3}$LLZO and $Ga_{0.2}Al_{0.2}$LLZO ^{27}Al spectra. The corresponding relative energies of selected configurations are compiled in Table 3 along with the key NMR properties and the structural data used

https://dx.doi.org/10.1021/jacs.9b12685
J. Am. Chem. Soc. 2020, 142, 3132−3148

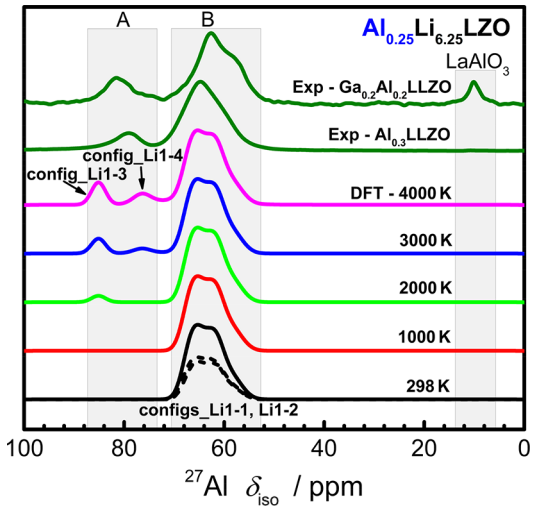

Figure 5. DFT/GIPAW ^{27}Al MAS NMR spectra of the single-doped cubic $Al_{0.25}Li_{6.25}LZO$ models compared to the experimental spectrum of the $Ga_{0.2}Al_{0.2}LLZO$ and $Al_{0.3}LLZO$ samples. The Boltzmann-weighted individual contribution from each energetically relevant defect configuration is considered in the convoluted DFT spectra and depicted for the 298 K case (dashed lines). The effect of higher-energy configurations on the spectrum was checked by considering temperatures of 1000−4000 K in the Boltzmann weighting. Gaussian broadening (Γ = 2 ppm) is used for all computed spectra.

for a local coordination analysis. The defect configurations are labeled based on their relative energies and the nature of the dopant and defect site (e.g., config_1Al/Ga-[X]-[1−16], with X being Li1, Li2, and La, depending on the defect site).

The low-lying configurations (i.e., thermally accessible, with ΔE_f < 0.5 eV/fu) involve the Al-doping of various Li1 sites, forming AlO_4 tetrahedra (Table 3). In the two almost-degenerate lowest-energy configurations (configs_1Al−Li1−1 and Li1−2), Al dopes into Li1 sites with similar coordination environments (Figure 6) giving ^{27}Al NMR shifts of δ_{iso} = 68.6 and 68.3 ppm, respectively. Their asymmetric coordination environments lead to large quadrupolar coupling constants (C_Q = 5.20 and 5.34 MHz) and large asymmetry parameters (η_Q = 0.74 and 0.67), resulting in broad and distorted line shapes similar to those found for the observed peak B (Figure 5).

To probe the source of the other observed peaks, we have also calculated the NMR resonances originating from the higher-energy Li1-defect configurations by scaling NMR contributions based on Boltzmann weights at elevated temperatures (1000−4000 K, Figure 5): A stepwise increase of the simulation temperature introduces two new ^{27}Al NMR peaks, originating from configs_1Al−Li1−3 and Li1−4 (with ΔE_f = 0.446 and 0.803 eV/fu), respectively. These configurations give rise to two additional sharper peaks located at 85.3 and 77.9 ppm, respectively, which are close in chemical shift to the observed peak A. The former peak (from config_1Al−Li1−3) has a chemical shift that is closer to that of the observed peak A from the $Ga_{0.2}Al_{0.2}LLZO$ sample (82 ppm), whereas the latter (config_1Al−Li1−4) is closer to that from the $Al_{0.3}LLZO$ sample (78 ppm) (Figure 5). Furthermore, these more symmetric local environments (see DI and BVS values, Table

Table 3. Local Coordination Analysis for the Al- and Ga-Doped Sites in the Selected Single-Doped Configurations ($Al_{0.25}Li_{6.25}Zr_2O_{12}$ and $Ga_{0.25}Li_{6.25}La_3Zr_2O_{12}$), along with Their ^{27}Al/^{71}Ga NMR Parameters and Relative Energies[a]

config ID	δ_{iso} [ppm]	C_Q [MHz]	η_Q	DI (×10^{-4}) B	DI (×10^{-4}) A	DI (×10^{-4}) E	BVS	ΔE [eV]
1Al Placed on Li1 Sites								
Li1-1	**68.6**	**5.20**	**0.74**	**0.4**	**4.6**	**3.2**	**2.53**	**0**
Li1-2	**68.3**	**5.34**	**0.67**	**0.3**	**4.7**	**3.3**	**2.53**	**0.01**
Li1-3	**85.3**	**0.95**	**0.42**	**0.1**	**0.6**	**0.4**	**2.64**	**0.45**
Li1-4	77.9	3.00	0.16	0.3	1.6	0.8	2.61	0.80
Li1-5	80.4	6.38	0.77	0.9	3.8	2.0	2.63	0.96
Li1-6	80.3	6.41	0.76	0.9	3.8	1.9	2.53	0.97
1Al on Li2 Sites								
Li2-1	81.2	13.6	0.16	1.2	12.0	7.5	2.44	1.39
Li2-2	70.1	14.5	0.53	1.5	13.6	8.7	2.35	1.44
Li2-3[b]	29.5	4.18	0.65	2.4	12.7	8.2	2.23	1.51
Li2-4[b]	29.4	4.52	0.64	2.5	12.7	8.3	2.22	1.51
1Ga Placed on Li1 Sites								
Li1-1	**189.1**	**10.2**	**0.48**	**0.3**	**5.9**	**4.1**	**2.70**	**0**
Li1-2	**187.7**	**10.4**	**0.50**	**0.4**	**6.1**	**4.2**	**2.70**	**0.01**
Li1-3	**166.0**	**10.7**	**0.39**	**0.2**	**6.0**	**4.2**	**2.70**	**0.29**
Li1-4	280.2	2.54	0.75	0.2	0.9	0.5	2.81	0.53
1Ga on Li2 Sites								
Li2-1[c]	**189.8**	**10.9**	**0.41**	**0.4**	**5.7**	**3.9**	**2.71**	**0.02**
Li2-2	158.1	26.5	0.61	1.9	14.9	9.4	2.51	1.22
Li2-3	157.8	26.3	0.56	1.8	14.7	9.3	2.51	1.23

[a]NMR parameters (chemical shift, δ_{iso}, C_Q, and η_Q), and local coordination parameters (distortion indices, DI, of bonds (B), angles (A), and polyhedral edges (E), and bond valence sum, BVS) are presented along with the relative energy, ΔE. Configurations are sorted based on their relative formation energies, and energetically most-relevant (low-lying) ones are indicated in bold. Complete lists of the Al- and Ga-doped configurations are given in Tables S7 and S8, respectively. [b]These configurations have 5-fold coordination, whereas all others listed here are of 4-fold coordination. [c]config_1Ga−Li2−1 is designed as a Li2-defected configuration, but Ga moved to a Li1 site in the structure optimization, lowering its relative energy compared to the other Li2-defected ones.

https://dx.doi.org/10.1021/jacs.9b12685
J. Am. Chem. Soc. 2020, 142, 3132−3148

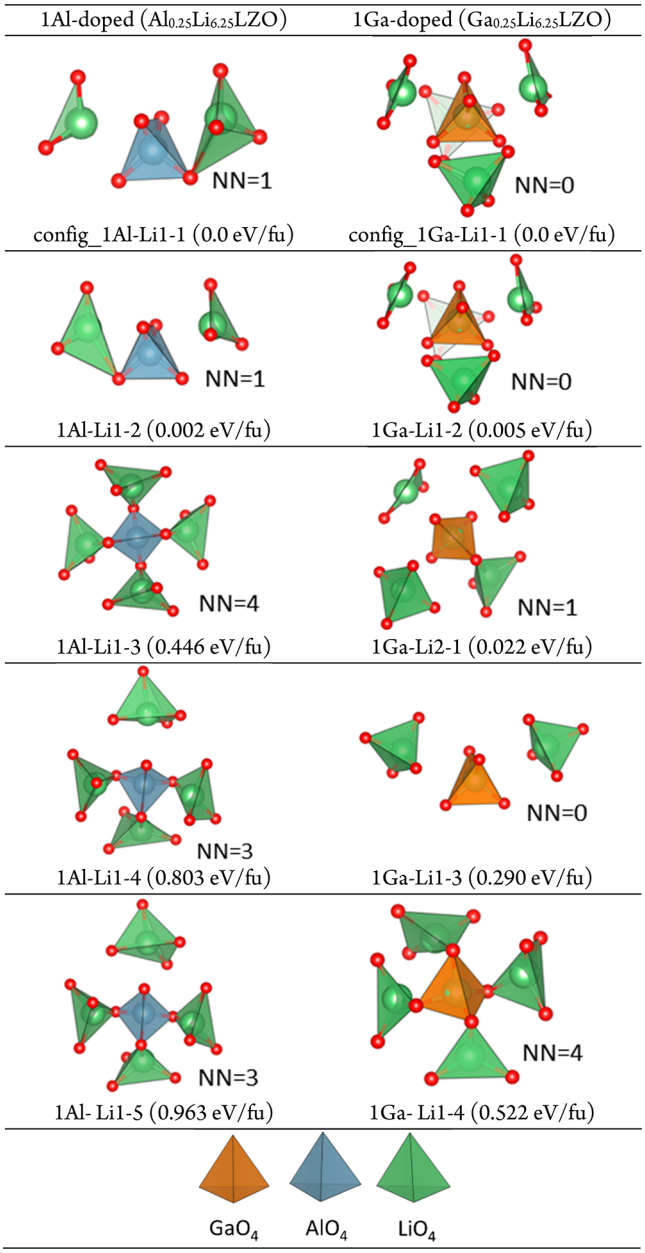

Figure 6. Local surroundings of the (left) Al and (right) Ga-doped sites in the selected single-doped defect configurations. Polyhedra vertices correspond to the coordinating oxygens. Relative energies are given in parentheses. The number of corner-sharing LiO_4 neighbors (NN) are also indicated, the Li ions formally corresponding to ions on the Li2/96h sites. Configuration label definitions are given in the text. The immediate LaO_8 and ZrO_6 neighbors of the dopant sites are depicted in Figures S14 and S15.

3) have low C_Q values (0.95 and 3.0 MHz for config_1Al−Li1−3 and Li1−4, respectively).

To explore the distinct doping site distortions, the first coordination shells of the AlO_4 sites were inspected (Figure 6, left panel): in general, all Li sites (hence, also the dopant sites) are surrounded by four oxygen/corner-sharing ZrO_6 and two LaO_8 sites, while the number of immediate LiO_4 (Li2) neighbors varies. Config_1Al−Li1−3 has a dopant site with the highest number of immediate Li neighbors and the lowest distortion among others (i.e., lowest DI and highest BVS values, Table 3). The other configurations, particularly configs_1Al−Li1−1 and Li1−2, have fewer corner-sharing LiO_4 neighbors (NN = 1), and are also highly distorted. The nearby small and polarizing Li atoms appear to play a crucial role in affecting the bonding: the AlO_4 sites, whose corner-sharing LiO_4 neighbors are missing, are forced into more distorted AlO_4 tetrahedra, resulting in higher C_Q values and hence broader NMR signals (Table 3).

To see if other high-energy Li1-defected configurations might contribute to the ^{27}Al MAS NMR spectrum, the GIPAW-NMR spectrum was also convoluted with equal contributions from each configuration (configs_1Al−Li1−1 to 12, Figure S16c). The addition of high-energy doped sites gives rise to extra features flanking the main feature in the 50−80 ppm region. Of these, config_1Al−Li1−5 and A6 yield NMR shifts (with $C_Q \approx$ 6.4 MHz) located around 70−75 ppm, similar to config_1Al−Li1−4. These peaks may be associated with the (occasional) minor shoulder observed between the peaks A and B (only present in the NMR spectrum of the $Al_{0.24}$LLZO sample). Note that this shoulder has also been associated with a nongarnet phase, γ-$LiAlO_2$.[19]

If the high-energy Li2-site configurations are included, corresponding to an out-of-equilibrium state (Figure S16d), a set of new peaks appear in the 15−40 ppm region of the predicted ^{27}Al NMR spectrum. Since none of the experimental spectra have signal intensity in this specified region, we again rule out the doping of Li2 (96h/48g) sites, even at higher doping levels (as well as the higher-energy Li1 sites with comparable E_f). Doping of La sites is predicted to produce peaks in the 35−0 ppm region (Figure S18a), characterized by high C_Q values (and thus very broad peaks). The sharp resonance sometimes seen in this spectral range at 12 ppm has too small a C_Q to be assigned to these high energy dopant configurations, consistent with its prior assignment to the nongarnet impurities in the sample, e.g., $LaAlO_3$.[3,19,23]

Next, we scrutinize the effect of higher doping levels on the computed ^{27}Al NMR line shapes, by adding more dopants to the supercell (i.e., double-, triple-, and quadruple-doped cases). As discussed in more detail in the SI (Figures S19 and S22), on going from the single-dopant case ($Al_{0.25}$LLZO) to the double-dopant cases ($X_{0.5}Li_{5.5}LZO$, where X = Al or Al + Ga), the main peak broadens further due to an increase in the C_Q (to ca. 7.1 MHz) and shows a characteristic SOQ splitting due to low EFG asymmetry parameter (η_Q = 0.01−0.02), predicted for both 2Al ($Al_{0.5}$LLZO) and 1Al + 1Ga-doped ($Al_{0.25}$ $Ga_{0.25}$LLZO) model systems (Table S9). The computed C_Q values are now larger than the experimentally determined values.

Visual inspection of the local arrangements at the dopant sites in the 2Al, $Al_{0.5}$LLZO model (Figure S23) reveals that the lowest-energy config_2Al-1 is in fact a combination of the two lowest-lying single-doped configurations (viz. configs_1Al−Li1−1 and Li1−2) with alike dopant-site local environments. In addition, these two dopant sites are close neighbors, indirectly connected through a LaO_8 site (Figure S23), and do not have oxygen-sharing LiO_4 neighbors as opposed to the single-dopant equivalents each with one LiO_4 neighbor (Figure 6 and Figure S23). This arrangement for Al gives rise to a higher C_Q (7.1 vs 5.2 MHz), once again underlining the regulatory role of the LiO_4 neighbors in controlling the local coordination of a dopant site. The very low EFG asymmetry (η_Q = 0.01−0.02) of the AlO_4 sites in the $Al_{0.5}$LLZO model can be attributed to a higher axial symmetry at each site, as endorsed by small distortion indices of bonds (Table S9). The findings for the $Al_{0.25}Ga_{0.25}$LLZO model are similar.

https://dx.doi.org/10.1021/jacs.9b12685
J. Am. Chem. Soc. 2020, 142, 3132−3148

3.2.2.2. Computed ^{71}Ga MAS NMR Spectra. A similar configurational analysis was performed for the Ga case, which endorses the proposed doping preference for the Li1 sites over the Li2 ones (see Table 3, and Table S8 for a complete list). A similar GaO_4 environment is formed in all three low-lying configurations (configs_1Ga−Li1−1, Li1−2, and Li2−1, Table 3, Figure 6). This gives rise to almost identical chemical shifts (δ_{iso} = 187−190 ppm), similarly large C_Q values (10.2−10.7 MHz) and medium η_Q values (0.39−0.50), all jointly contributing to the lower frequency (SOQ) line shape, which closely resembles the experimentally observed peak B (Figure 7).

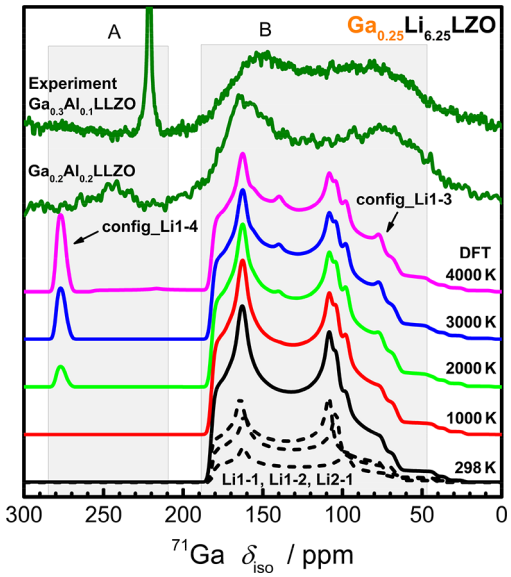

Figure 7. DFT/GIPAW ^{71}Ga MAS NMR spectrum of the single-doped cubic $Ga_{0.25}Li_{6.25}LZO$ models compared to the experimental spectrum of the $Ga_{0.3}Al_{0.1}LLZO$ and $Ga_{0.2}Al_{0.2}LLZO$ samples. The Boltzmann-weighted individual contribution from each energetically relevant defect configuration is considered in the convoluted DFT spectra and depicted for the 298 K case (dashed lines). The effect of higher-energy configurations on the spectrum was checked by considering temperatures of 1000−4000 K in the Boltzmann weighting. Gaussian broadening (Γ = 2 ppm) is used for all computed spectra.

The large C_Q and η_Q values of the broad feature can be ascribed to the distorted GaO_4 environments in lowest-energy configs_1Ga−Li1−1, Li1−2, and Li2−1 (Table 3). Reminiscent of the Al-doped case, in these low-lying Ga-doped configurations, the LiO_4 tetrahedra that surround the dopant GaO_4 sites (i.e., their oxygen-sharing neighbors) are highly distorted or missing (their coordination shells are visualized in Figure 6). As compared to the ^{27}Al, the ^{71}Ga NMR shows a much broader SOQ line shape, due to the larger C_Q, arising from the higher quadrupolar moment of the ^{71}Ga isotope.

Increasing the simulation temperature leads to the inclusion of higher-energy Li1-substituted configurations, particularly configs_1Ga−Li1−3 and Li1−4, in the convoluted ^{71}Ga NMR spectrum (Figure 7). The low C_Q value (2.54 MHz) of config_1Ga−Li1−4 results in a sharp resonance in the simulation, in agreement with observed peak A. As in the Al-doped case, this low C_Q is ascribed to the higher symmetry of the GaO_4 environment (with lowest DI values, Table 3). This is facilitated by the four immediate Li neighbors (Figure 6), which donate equivalent (balanced) bonded Li−O interactions and thus do not distort the GaO_4 tetrahedron significantly. The chemical shift of config_1Ga−Li1−4 (δ_{iso} = 280.2 ppm) is noticeably higher than configs_1Ga−Li1−1 to 3, and while it is in the same region as peak A, it is noticeably larger, the experimental values being seen at 220 and 220−240 ppm for $Ga_{0.3}Al_{0.1}$ LLZO and $Ga_{0.2}Al_{0.2}$LLZO samples, respectively.

On account of its rather high formation energy (E_f = 0.528 eV/atom), config_1Ga−Li1−4 is expected to be present only at a higher level of doping or in a sample quenched from high temperature. This may be one reason for the varying height of the experimental peak A (Figure 3), from sample to sample. By contrast, config_1Ga−Li1−3 is more likely to be populated, with its lower E_f of 0.290 eV/fu, and it leads to a resonance associated with a slightly larger C_Q of 10.7 MHz than configs_1Ga−Li1−1 and Li1−2, but similar to Li2−1. This peak may contribute to the right-hand shoulder of the observed peak B, suggesting that local disorder controls the broadening of the lower frequency discontinuity of the SOQ line shape.

The addition of significant contributions from the other higher-energy Li1 doping configurations broaden and shift the position of the lower frequency discontinuity of the SOQ line shape (as illustrated in Figure S17c) with equal weighting for all configurations. The resulting spectrum improves the fit to the experimentally measured spectrum of $Ga_{0.3}Al_{0.1}$LLZO (Figure 3a and Figure S17c). While these defect configurations are thermally less accessible due to their high formation energies, it is clear that more disorder is present in these samples than captured by the two lowest-energy configurations alone.

The ^{71}Ga NMR spectra from the higher Ga-doping levels and local coordination analysis reveal characteristic trends in NMR properties, and their structural origins, which are analogous to the ^{27}Al case, e.g., a higher C_Q (12.5 vs 10.2 MHz) and very low η_Q (0.01−0.02), stem from the missing LiO_4 neighbors. An in-depth discussion is given in the SI, Part 6a.

The general notion that a more distorted dopant site promotes a higher C_Q value is validated for the Al- and Ga-doped cases by plotting the C_Q values against the distortion indices (DIs) of bond lengths, angles, and tetrahedron edges (Figure 8). Similarly, a clear correlation is observed with C_Q increasing with increased quadratic elongation and with decreasing BVS (Figure S25).

3.2.2.3. Computed ^{17}O MAS NMR Spectra. Calculations were performed to assign the characteristic peaks seen in the ^{17}O spectra of Figure 4 and are compared with the experimental reference ($Ga_{0.2}Al_{0.2}$LLZO sample). Only the low-energy configurations at each doping level were used to generate the spectra shown in Figure 9. The effect of including the higher-energy defect configurations (for single-doped Al/Ga cases) is shown in the SI, Figure S26.

Figure 9 shows that the undoped c-LLZO yields the fewest features and is dominated by two resonances with similar shifts which are close to those of the observed peak IV, whereas the other peaks are either much weaker (corresponding to peaks I−III) or completely missing (peak V). On increasing the doping level, the main peak IV becomes progressively weaker, while the other peaks become more pronounced, except for the peak at around 380 ppm. No peaks are predicted with a shift similar to this measured signal, consistent with its assignment to a background signal (ZrO_2 or $La_2Zr_2O_7$).[81,90] The predicted decrease in relative intensity of peak IV (Figure 9 and Figure S27) at higher doping concentrations suggests that this peak may correspond to the ^{17}O resonances originating from the OLi_x sites, whose relative amount decreases upon Al/Ga doping.

https://dx.doi.org/10.1021/jacs.9b12685
J. Am. Chem. Soc. 2020, 142, 3132−3148

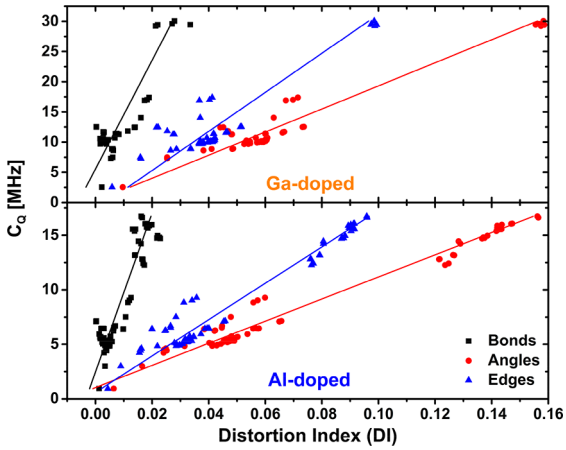

Figure 8. Local coordination analysis for the Ga- or Al-doped Li1 sites from all single- and double-doped configurations. Correlation between the quadrupolar coupling constants (C_Q, MHz) and distortion indices (DI, defined in eq 2) of bond lengths, angles, and polyhedral edges is given as a measure of the deviation from the tetrahedral coordination of a given Al/Ga dopant site.

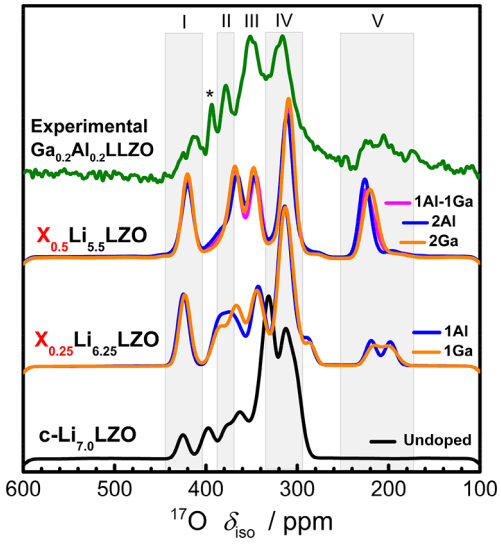

Figure 9. Influence of the Al and Ga dopants on the computed GIPAW ^{17}O NMR spectra of cubic LLZO variants compared to the experimental spectrum of the $Ga_{0.2}Al_{0.2}$LLZO sample. The undoped, single- and double-doped cases are shown, and the higher-doping levels are given in Figure S27. The computed spectra contain contributions from multiple defect configurations (accessible at 298 K). Gaussian broadening (Γ = 8 ppm) is used for all computed spectra. The labels I–V indicate the experimental LLZO peaks and * ZrO_2 peak.

Noticeably, the calculated increase in the lowest-frequency peak at the increased doping levels suggests that the experimental peak V originates from the oxygens coordinating the dopant sites. Relevantly, the doping of the higher-energy Li1 sites is associated with a broadening of peak V (Figure S26). By contrast, experimental peaks at 170, 575, and 625 ppm are not predicted in the DFT/GIPAW results (Figure 9), suggesting that these peaks stem from the nongarnet impurities in the sample, as described above. Very similar ^{17}O NMR spectra are predicted for spectra with the same dopant concentration, independent of whether the dopant is Al or Ga. In contrast, the number of dopants and their distribution within the LLZO lattice have a more discernible effect (Figure 9). No clear distinction for the site preference of the Al or Ga dopants for either Li1 and Li2 can be made using the ^{17}O NMR data (Figure S31), as the oxygen atoms coordinated to Al/Ga substituted on either the Li1- or Li2-defected sites both give rise to predicted shifts similar to those of peak V.

The NMR properties (δ_{iso}, C_Q, and η_Q values) and coordination environments for selected defect stoichiometries and configurations are collated in Table 4. The additional peaks at 200–230 ppm (matching with the observed peak V, Figure 9) originate from the oxygens coordinating the Ga/Al dopant atom(s), with the shortest interatomic distances (D(Al–O) = 1.80 Å and D(Ga–O) = 1.88 Å), further corroborating the assignment of peak V to the dopant sites. The ^{17}O signals originating from the dopant sites have larger C_Q values compared to those from the other sites. Relevantly, the oxygens at the GaO_4 sites display larger C_Q values than the AlO_4 sites (3.50–3.64 vs 1.06–1.36 MHz), which could be attributed to the larger covalency of the Ga–O bonds than the Al–O ones.

From the local coordination analysis (Table S11), we note that every oxygen has one to six Li atoms within 3.6 Å, along with Zr and two La neighbors; the closest neighbor is always a Li atom (except for when replaced by a dopant). The differences in NMR properties of oxygens can be attributed to the number of their Li/dopant neighbors, lower shifts generally correlating with Li–O bonds.

Examining Table 4 and Table S10, a noticeable grouping of the oxygen sites for the double-doped cubic-LLZO cases (viz. 2Ga, 1Ga + 1Al, and 2Al-doped with the $X_{0.5}Li_{5.5}$LZO stoichiometry) is seen, which can be ascribed to the less diversity in oxygen local environments in the respective lowest-energy configurations (see Figure S23). These structures are not only useful for a clearer assignment of local environments in c-LLZO (due to the more distinctive oxygen grouping) but also give a good overall match with the experimental spectrum (Figure 9 and Figure S28), increasing the accuracy of peak assignments. For discussion, only the 1Ga + 1Al-doped case was picked, the other two having similar NMR properties and oxygen groups (Table S10).

The oxygen sites in $Ga_{0.25}Al_{0.25}Li_{5.5}$LZO can be divided into six distinct groups (Table 4). The O1 group is coordinated to the dopant sites and leads to the 228–229 ppm peaks, matching with the observed peak V. Groups O2 and O3 are responsible for the resonances at 306–307 and 310–313 ppm, overlapping with the peak IV. These O2 and O3 oxygen sites all have three Li neighbors within bonding distance (2.6 Å), while their two closest neighbors are Li atoms which lie within the typical tetrahedral LiO_4 coordination distance (2.00 Å).[91] In contrast, the Li–O distances are longer for the other oxygen groups, yielding increasingly higher ^{17}O shifts. On this basis, peak IV can be primarily ascribed to the OLi_x polyhedra, in line with our earlier assignment. The O4 and O5 groups correspond to the 344–347 and 368–369 ppm peaks, which coincide with the measured peaks III and II, respectively. A common feature of these oxygen groups is fewer (two) first-coordination Li neighbors and longer Li–O distances, and shorter average distances to the Zr and La neighbors. No clear distinction can be made based on interatomic distances for these oxygen groups, suggesting that the OLi_x, OZr, and OLa_2 environments all contribute to the experimental peaks II and III. In contrast, the O6 group oxygens give the 419–422 ppm peak, showing a good match with the observed peak I. These oxygens have the closest proximity to the Zr and La atoms (shortest among all groups,

https://dx.doi.org/10.1021/jacs.9b12685
J. Am. Chem. Soc. 2020, 142, 3132–3148

Table 4. Local Coordination Analysis for the Distinctive Oxygen Atom Groups in c-LLZO Variants along with Their ^{17}O NMR Parameters (Isotropic Chemical Shifts, δ_{iso}, Quadrupolar Coupling, C_Q and EFG Asymmetry, η_Q)[a]

oxygen group	δ_{iso} [ppm]	C_Q [MHz]	η_Q	average D(O−O) [Å]	average D(O−La) [Å]	average D(O−Zr) [Å]	minimum D(O−Li)[b] [Å]	no. bonded Li neighbors	average D(O−X) [Å]
					c-Li_7LZO				
O1	296−307	0.62−1.34	0.15−0.99	3.04−3.08	2.57−2.71	2.14−2.21	1.89−1.95	3	
O2	313−316	0.65−0.97	0.41−0.99	3.04−3.07	2.59−2.62	2.13−2.16	1.89−1.92	3	
O3	326−340	0.61−1.22	0.35−0.98	3.06−3.08	2.58−2.62	2.09−2.16	1.86−1.93	2	
O4	344−345	0.74−1.11	0.18−0.79	3.08−3.09	2.54−2.60	2.10−2.12	1.85−1.87	2	
O5	352−357	0.84−0.99	0.10−0.60	3.07−3.09	2.56−2.58	2.10−2.13	1.88−1.93	2	
O6	362−372	0.93−1.39	0.16−0.91	3.07−3.11	2.55−2.57	2.07−2.09	1.82−1.94	2	
O7	379−381	0.83−1.53	0.48−0.53	3.10−3.13	2.52−2.61	2.09−2.13	1.96−2.07	2	
O8	395−403	0.36−1.33	0.20−0.59	3.09−3.11	2.49−2.55	2.08−2.10	1.99−1.86	1	
O9	425−426	1.14−1.17	0.17−0.38	3.10−3.11	2.52−2.54	2.07	2.00−2.01	1	
					1Ga-Doped (c-$Ga_{0.25}Li_{6.25}$LZO)				
O1a	206	3.50	0.08	3.06−3.07	2.65−2.66	2.18		0	1.87
O1b	224	3.50	0.37	3.07−3.08	2.63	2.21		0	1.88
O2	286	0.94−0.99	0.98	3.06	2.67	2.13	1.90	3	>3.6
O3	303−320	0.6−1.0	0.29−0.94	3.04−3.08	2.57−2.63	2.12−2.17	1.89−1.92	2−3	>3.6
O4	337−350	0.9−1.1	0.31−0.58	3.06−3.07	2.58−2.63	2.08−2.17	1.92	2	>3.6
O5	363	0.99−1.01	0.12−0.15	3.09	2.58	2.09	1.92	2	>3.6
O6	371−373	1.06−1.13	0.10−0.78	3.09	2.55−2.57	2.08−2.09	1.92−1.93	2	>3.6
O7	380	0.82	0.30	3.08	2.52	2.10	1.84	1	>3.6
O8	389	0.75	0.77	3.09	2.50	2.08	1.81	1	>3.6
O9	423−426	1.05−1.18	0.28−0.43	3.10	2.51−2.53	2.07−2.09	1.99−2.02	1	>3.6
					1Ga + 1Al (c-$Al_{0.25}Ga_{0.25}Li_{5.5}$LZO)				
O1a (Al-crd.)	228−229	1.36	0.54	3.03	2.64	2.17		0	1.80
O1b (Ga-crd.)	228−229	3.64	0.19	3.06	2.63	2.17		0	1.88
O2	306−307	0.57−0.58	0.57−0.61	3.05	2.60	2.16	1.90	3	>3.6
O3	310−313	0.55−0.84	0.58−0.76	3.06	2.59	2.16	1.91−1.92	3	>3.6
O4	344−347	0.83−0.88	0.32−0.38	3.06	2.60	2.11	1.92	2	>3.6
O5	368−369	0.95−1.00	0.21−0.30	3.08	2.57	2.07	1.93−1.94	2	>3.6
O6	419−422	1.05−1.09	0.35−0.41	3.08	2.52−2.54	2.07	1.99	1	>3.6

[a]Covalent radii of the atoms in a given pair are considered for determining the oxygen neighbors. δ_{iso} values are referenced using σ_{ref} = 242 ppm. For brevity, only the minimum-energy configuration of each stoichiometry and only the selected stoichiometries are shown. A complete table containing all relevant configurations and other LLZO stoichiometries are given in Table S10. Oxygen sites are grouped based on their NMR properties as individually documented in Table S11. [b]Minimum Li−O distances are listed instead of the average D(Li−O) values, which are scattered due to varying number of Li neighbors (see Figure 10b). A range of values is given for some of the NMR parameters and the interatomic distances; this follows from the minor variations in these values for the individual oxygen atoms from the same group with similar properties, due to small variations in the local structures of the specific environments.

2.52−2.54 and 2.07 Å, respectively), only one bonded Li neighbor, and the longest Li−O distances.

For the undoped and two single-doped (1Al and 1Ga) c-LLZO cases with more distorted crystal sites, the oxygens are highly scattered in terms of NMR properties (Table 4 and Table S10, also see Table S11 for all individual oxygen sites). In all three cases, the oxygen sites can be grouped into at least 9 groups, with large deviations in δ_{iso}, C_Q, and η_Q values that diminish the accuracy in peak assignments. In general, there is a notable similarity in terms of NMR properties between the two sets of oxygen groups from the two single-doped (1Al and 1Ga) cases, except for the ones coordinating the dopants directly. This finding suggests that the main features (peaks I−IV) are not affected by the dopant type, as they are produced by the oxygens found in the LLZO lattice, viz. primarily coordinating the Li, La, and Zr sites (as noted above).

A comparison of the predicted ^{17}O chemical shifts and the average bond lengths of diverse types reveals a clear trend of higher ^{17}O NMR shifts at longer O−O interatomic distances and shorter Zr−O and La−O distances (Figure 10a), consistent with the link between peak I and the oxygens coordinating the La and Zr sites more closely (as previously noted). Conversely, no clear trend can be spotted for the average Li−O distances, as the immediate Li neighbor counts of the oxygen atoms vary significantly. Grouping the Li−O distances based on the number of Li neighbors, however, reveals a correlation between decreasing chemical shift and shorter Li−O distances for each group (Figure 10b). The latter finding agrees well with our previous assignment of peak IV primarily to the OLi_x (x = 1−4) sites. As also visible from Figure 10b, the dopant−oxygen distances (D(X−O), where X = {Al, Ga}) are in the range 1.80−1.88 Å (in line with the lowest-energy configurations, compiled in Table 4), and the corresponding chemical shifts range from 160 to 240 ppm, linked to peak V. Relevantly, no clear correlation was observed between the number of Li−O bonds and the ^{17}O NMR shifts, as the oxygen groups with a different number of Li neighbors have similar distribution of chemical shifts (ranging from 275−300 to 450 ppm, Figure 10b, except for 1Li-neighbor ones with a single data point).

https://dx.doi.org/10.1021/jacs.9b12685
J. Am. Chem. Soc. 2020, 142, 3132−3148

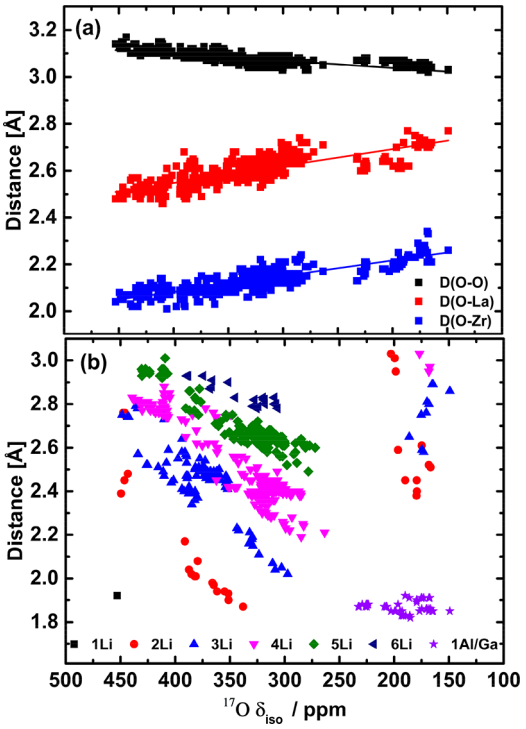

Figure 10. Local coordination analysis for the oxygen sites. Correlation between ^{17}O chemical shifts (δ_{iso}) and various types of average interatomic distances: (a) D(O−O), D(O−La), and D(O−Zr) and (b) D(O−Li) and D(O−{Al/Ga}), considering the distances within 3.6 Å. In part b, D(O−Li) values are grouped based on the Li neighbor counts of oxygens ("1−6Li") and the dopant−oxygen distances are also shown ("1Al/Ga", purple stars). For clarity, only the single Al/Ga-doped configurations are shown. A complete analysis including all possible configurations can be found in Figures S29 and S30, which exhibit identical trends as the ones shown here.

4. DISCUSSION

There is an ongoing debate in the literature concerning the site preference of Al/Ga dopants inside the c-LLZO framework and its connection to the observed NMR resonances (see the SI, Part 7, for an overview). Tables S12 and S13 give a comparison of the current computed and experimental ^{27}Al and ^{71}Ga NMR peak positions, (fitted and predicted) NMR parameters, and site-assignments with those previously reported. This comparison reveals overall a good agreement between these two data sets.

More specifically, we observe two characteristic features in both ^{27}Al and ^{71}Ga NMR spectra (denoted as peaks A and B). Our predicted and experimental spectra reproduce the common broad peak B in both ^{27}Al and ^{71}Ga NMR spectra (at 68 and 193−199 ppm, respectively). Our DFT predictions suggest that peak B results from multiple defect configurations with distorted tetrahedral AlO_4 or GaO_4 coordination (at the Li1/24d sites), leading to a relatively large C_Q (^{27}Al, 5.3 MHz; and ^{71}Ga, 10.2−10.9 MHz) and η_Q (^{27}Al, 0.74; and ^{71}Ga, 0.39−0.50) values. These findings align well with our experiments and previous reports.[3,20,23,27] However, our ^{27}Al results contradict the DFT predictions by Rettenwander et al.,[24] who reported very small calculated C_Q and η_Q values (0.8 MHz and 0.1) for the 68 ppm ^{27}Al peak, which could be linked to a "perfect" (nondistorted) tetrahedral Li1/24d site, rather than a distorted one, and would lead to a very sharp peak, as opposed to the observed 68 ppm broad feature.

Our DFT predictions on a higher doping level, i.e., the double Al-doped cases (i.e., $Al_{0.5}Li_{5.5}LZO$), suggest that the minimum-energy defect configuration yields an ^{27}Al resonance with even larger C_Q (7.1 MHz) and lower asymmetry (η_Q = 0.02) than the single-doped case. The predicted high quadrupolar coupling and high axial EFG symmetry combination is in line with some previous reports,[3,20] albeit at a lower chemical shift. Similarly, the double-Ga doping ($Ga_{0.5}Li_{5.5}LZO$) leads to an even larger C_Q (12.5 MHz) and an almost zero EFG asymmetry ($\eta_Q \leq$ 0.02), in good agreement with Bernuy-Lopez et al.[27] As previously described, the double-doped lowest-energy defect configurations (in both the Al- and Ga-doped cases) accommodate two identical, highly distorted Li1/24d dopant sites that are connected through a LaO_8 site. In addition, all oxygen-sharing LiO_4 neighbors (that were present in the individual single-doped cases) are missing, contributing to the distortion of the AlO_4/GaO_4 sites and thus their higher C_Q value (^{27}Al, 7.1 vs 5.3 MHz; and ^{71}Ga, 10.2−10.9 vs 12.5 MHz). These computational findings suggest that not only the doping site but also its oxygen-sharing neighbors (second coordination shell) will influence the observed NMR signals. This may explain the high diversity in the observed NMR parameters for the corresponding broad ^{27}Al and ^{71}Ga peaks (B).

Multiple dopant sites with slightly different environments are expected to contribute to the SOQ discontinuity (shoulder) of peak B and the smoothing of the singularities and inflections. The effect of the structural disorder on the NMR spectra can be captured by explicitly considering multiple defect configurations (as done here) or by using the Maurer[92] or Czjzek[93] models to simulate the joint density distributions arising from the disorder sites. Relevantly, using these models, local disorder in crystal structure was linked with an extended right-hand tail observed in the ^{27}Al NMR spectra for the analogous AlO_x environments in other solid systems,[94,95] and also in the ^{71}Ga NMR spectra of similar GaO_x environments.[96,97] Given these detailed studies, structural disorder effects are considered in our spectral simulations only in the form of sampling of diverse configurations. One should note that the disorder entropy contributions to the relative energies of configurations are negligible (see the SI, Part 5) and that smoother spectra could be obtained by sampling more defect configurations using a larger simulation cell.

A second resonance (peak A) is observed for both ^{27}Al and ^{71}Ga NMR in the 74−81 and 222−239 ppm regions, respectively, for samples of diverse stoichiometries, in line with previous experimental reports (^{27}Al refs 3, 18, 19, and 23 and ^{71}Ga refs 22, 23, and 26−28). Based on our DFT results, these sharper peaks are linked with low C_Q values (^{27}Al, 0.95 MHz; and ^{71}Ga, 2.54 MHz). For both ^{27}Al and ^{71}Ga NMR, we ascribe this weak quadrupolar coupling to a nondistorted tetrahedral coordination, stemming from the high symmetry of the doped site and the four corner-sharing LiO_4 neighbors (NN = 4, Figure 6). Therefore, peak A is likely to originate from the doping of perfect (nondistorted) tetrahedral Li1/24d sites, rather than the distorted 4/5-fold coordinated Li2/96h, 6-fold coordinated Li2/48g, or La sites, contradicting the previous assignments of this resonance made in the literature.[3,18,19,22−24,28] Relevantly, Al and Ga dopants sitting at the Li2 or La sites are predicted to yield ^{27}Al and ^{71}Ga signals at very low chemical shifts, in a range that is not observed experimentally, and the corresponding defect configurations have notably higher formation energies, rendering them thermally inaccessible (even at high synthesis/sintering temper-

https://dx.doi.org/10.1021/jacs.9b12685
J. Am. Chem. Soc. 2020, 142, 3132−3148

atures). This finding agrees well with the general notion that Ga in a tetrahedral environment will be in the range 107−222 ppm, whereas in an octahedral environment will be between 80 and −42 ppm.[67,77]

We note that lower dopant levels would increase the probability that a dopant atom is surrounded by four Li ions (NN = 4, yielding a higher peak A). The sample $Al_{0.15}$LLZO with the lowest doping level (having the highest Li content) is associated with the highest intensity of peak A. This suggests that the formation of two distinct local environments likely depends on the number of Li-ion neighbors. Moreover, a wide range of peak A:B intensities are obtained for samples with a dopant level of $X_{0.4}$ (X = Al/Ga), suggesting a nonrandom distribution of Li ions on the Li2 sites. Relevantly, we show that having four Li2 neighbors at the higher (double) doping level leads to a higher energy penalty (see Figure S24), in line with the decreased availability of Li sites. Based on these findings, we speculate that, at the lower concentrations, Al/Ga is largely randomly substituted in the lattice, creating regions where the dopants are closely packed (like in our double-doped models). This will push the Li ions away from these clustered dopants, causing them to increasingly find places near the isolated dopants, thus increasing the fraction of the dopant sites with 4 Li neighbors (NN = 4). Due to the computational costs of the NMR calculations, our simulation cells were kept small, mainly allowing for the modeling of isolated dopants. A more accurate sampling of such dopant clusters will be possible through cluster expansion analysis or large-scale MD simulations using interatomic potentials (as done in ref 40). We are currently exploring the effect of a wider range of compositions and synthesis conditions on the relative A:B peak intensities.

The defect configurations associated with peak A are predicted to have a higher formation energy as compared to those linked with peak B (yet still much lower than the La- or Li2-defected ones). Accordingly, we had to use unphysically high (model) temperatures in the Boltzmann weighting (e.g., up to 4000 K) to account also for these higher-energy configurations in the NMR spectra. However, we note that these DFT-based simulation temperatures should not be taken as absolute temperatures, because small errors in the relative energies of the clusters even within the errors of DFT cause large errors in temperature estimations. Instead these simulations demonstrate that these distinctive local environments can result from quenching in different configurations. We also note that the predicted peak A in both ^{27}Al and ^{71}Ga NMR spectra is somewhat shifted with respect to the corresponding experimental sharp peaks. This is likely due to the different dopant stoichiometries of the models/samples used for obtaining the computed/experimental spectra. As shown for the double-doped cases, the (indirect) interactions between the adjacent dopant sites might also play a role in the chemical shift of the peak A.

Based on our elaborate structural and spectral analysis (Figure 9 and Table 4), the characteristic ^{17}O NMR signals were assigned to specific crystallographic sites. In particular, the lower-frequency peak V (180−220 ppm) can be clearly linked to the oxygens coordinating a dopant site, based on its absence in the spectra of undoped c-LLZO and its broadening upon the inclusion of higher-energy dopant sites (Figure 9 and Figure S26). In contrast, the lower-frequency peak IV (320 ppm) can be primarily assigned to the oxygens in OLi_x environments, as corroborated by the decrease in its relative height at increasing doping levels and shorter interatomic distances (D(Li−O), Figure 10). Similarly, the higher-frequency peak I (420 ppm) can be assigned to the oxygens more closely coordinating the La and Zr sites, whereas the other observed signals II and III (378 and 352 ppm) likely have mixed contributions from the Li, La, and Zr sites. In contrast, all other observed signals can be assigned to the nongarnet impurities. Interestingly, the choice of the dopant has only a limited effect on the overall ^{17}O NMR predicted spectra, whereas the doping level is a more determining factor. Furthermore, the ^{17}O NMR data cannot be used to determine a site preference (Li1 vs Li2) for the Al or Ga doping (Figure S31), unlike the ^{27}Al and ^{71}Ga NMR spectra.

The dopant site preference has potential implications on the ionic transport mechanisms. Previous experimental and computational studies have corroborated the involvement of both Li1/24d and Li2/96h sites in the Li-conduction in diverse Al-, Ga-, and Mo-doped c-LLZO compositions.[9,23,40,43,45,98−100] Particularly, the spin-alignment echo (SAE) ^{6}Li NMR measurements revealed higher activation barriers for the 24d−24d Li-ion hopping (inevitably via a 96h site) compared to the other routes between two 96h sites (via the corners of Li1−O_4 polyhedra),[100] hinting at the doping preference for Li1/24d sites.

Relevantly, there are distinct views on the blocking or aiding effect of a dopant at the Li1/24d site on the Li conductivity. For instance, DFT calculations by Rettenwander et al.[43] indicated that a Ga/Al dopant placed at a Li1 site increases the site energy of the neighboring 24d site (while Ga^{3+} is providing a larger destabilization than Al^{3+}). This would decrease the potential energy difference between the neighboring tetrahedral and octahedral sites and, hence, enhance the Li diffusion. In contrast, based on MD simulations using interatomic potentials, Garcia Daza et al.[40] argued that a Ga/Al dopant sitting at a Li1/24d site would block the 24d junctions nearby (within 4 Å) and trap its associated Li vacancies at any substituent concentration. The authors also proposed that Li diffusion is completely hindered at high dopant levels (beyond the level required for stabilizing the cubic phase, i.e., Li_xLZO, $x < 6.5$), due to the synergistic effects, i.e., multiple dopants within 8 Å from each other.

Despite these contradictory findings regarding the influence of doping on the Li1/24d sites, it is clear that an efficient Li-ion conduction within LLZO would involve the octahedral Li2/96h sites. Based on our NMR results, we rule out the possibility of the Li2-substitution that would block Li migration, and we reveal the disparate local environments within and around the Li1 sites, the exact effect of which on the conduction is yet to be explored and is now under investigation in our group.

5. CONCLUSIONS

Local coordination environments in the undoped and Ga/Al-doped cubic-LLZO garnets were studied using *ab initio* calculations, whereas the predicted solid-state ^{27}Al, ^{71}Ga, and ^{17}O NMR spectra were analyzed in connection to the experimentally observed characteristic MAS NMR signals. In this regard, this study also reports the first measurement of the ^{17}O MAS NMR spectra of Al- and Ga-doped c-LLZO. The ^{17}O NMR spectra feature one distinct resonance that is linked with Al/Ga doping.

More specifically, a comprehensive and computationally extensive defect configuration analysis was performed, whereby each Li1, Li2, and La site in a primitive unit cell of cubic LLZO were explicitly considered with varying levels of Al and Ga dopants into to the lattice (X_aLi_{7-3a}LZO, where a = 0.0−1.0). The ^{27}Al, ^{71}Ga, and ^{17}O MAS NMR spectra were computed

https://dx.doi.org/10.1021/jacs.9b12685
J. Am. Chem. Soc. 2020, 142, 3132−3148

using DFT/GIPAW for the resulting symmetrically irreducible set of configurations. The contribution of each configuration with a specific stoichiometry to the NMR spectra was considered based on the Boltzmann weights at varying temperatures. The predicted spectra are in good agreement with the current and previous experimental observations, allowing for an accurate assignment of the peaks to the crystal sites in different configurations. Combining the current experimental and computational results, the following key conclusions were drawn:

1. Configuration analysis revealed that multiple defect configurations are thermally accessible and jointly contribute to the experimental NMR spectra. Doping of the Li1 sites is energetically more favorable than the Li2 and La sites, and only the calculated ^{27}Al and ^{71}Ga chemical shifts of the Li1-defected configurations are observed experimentally.
2. Two distinctive features are observed for both ^{27}Al and ^{71}Ga NMR spectra: (1) a broad peak, associated with a high quadrupolar coupling constant (large C_Q), which is attributed to the doping of the low-energy, highly distorted tetragonal GaO_4/AlO_4 sites, and (2) a sharper peak (due to much lower C_Q) at a higher chemical shift, associated with the doping of the higher-energy, highly symmetric (less distorted) dopant sites; other signals are due to nongarnet impurities. The higher-energy sites may be accessible at high synthesis temperatures (combined with rapid cooling) or thermodynamically stabilized with more dopants (per unit cell) at higher doping levels.
3. Both the sharp and broad features in ^{27}Al and ^{71}Ga NMR spectra are predicted to stem from 4-fold coordinated (Li1/24d) doped sites with varying local distortions, whereas the 5/6-fold (Li2/96h/48g) ones are energetically inaccessible and not experimentally observed (as opposed to some previous reports). This Li1 dopant site preference is in line with the proposed Li-ion conduction pathways involving the Li2/96h sites. The distorted nature of the dopant site is predicted to be controlled mainly by the oxygen-sharing Li2 neighbors. A general trend is revealed for both ^{27}Al and ^{71}Ga shifts, whereby the higher distortion of a dopant site links to a higher C_Q value.
4. The intensity of sharp peak A is likely to be controlled by the number of occupied Li2 site neighbors, sharing an oxygen with the dopant site. The highest A:B intensity is observed at the lowest doping level in line with the increased occupation of Li2 sites. The (indirect) effect of Li2 sites on Li-ion conduction is under further investigation.
5. Analysis of the higher dopant-level models suggests that multiple Al or Ga dopants in a crystal tend to form clusters at adjacent Li1 sites, pushing away the nearby Li (i.e., blocking access to the adjacent Li2 sites). In absence of Li neighbors, other nearby sites, e.g., ZrO_6 and LaO_8, mainly affect the local order at the individual dopant sites through the shared oxygen vertices, thus influencing the NMR parameters originating from the dopant site.
6. Using the experimental data, the predicted ^{17}O NMR spectra were validated, and the observed peaks were linked with the specific oxygen types coordinating the Li, Zr, and La sublattices. As compared to the ^{27}Al and ^{71}Ga cases, it was not always trivial to make clear assignments due to the shared nature of the oxygen atoms.
7. The right-hand-side (lowest frequency) ^{17}O peak (at 180−220 ppm) can be clearly related to the Al/Ga doping (i.e., oxygens coordinating the dopant), since it is missing in the undoped c-LLZO case, and its relative height increases on increased doping levels. DFT calculations also suggest that this peak is broadened upon doping of the higher-energy Li sites. The dopant type (Al or Ga) has a minor effect on the overall shape of the ^{17}O NMR spectra, while the number of dopants and their distribution within the LLZO lattice have a more discernible influence.
8. Coordination analysis revealed that each oxygen atom has one Zr and two La neighbors in its first coordination shell, while the number of immediate Li neighbors differs, giving rise to characteristic NMR parameters. Another key factor is the varying interatomic distances between oxygens and other atom types: the shorter Li−O distances are linked with lower chemical shifts, whereas the shorter Zr−O and La−O distances are predicted to lead to higher shifts. Based on these trends, the lower-frequency peak at ca. 320 ppm can be primarily assigned to the OLi_x (with x = 1−4) sites, as corroborated by the decrease in its relative height on higher doping levels. Similarly, the higher-frequency peak at around 420 ppm is predicted to originate from the oxygens more closely coordinating the La and Zr sites.

In light of the presented comprehensive atomistic insights corroborated by the experimental findings, this study is expected to clarify the ambiguities in the understanding of the links between the observed ^{17}O, ^{27}Al, and ^{71}Ga NMR signals and the local coordination environments in c-LLZO, which is a promising solid electrolyte candidate. The atomistic insights into the dopant site preference, the local coordination environments in the Li1 dopant sites, and the closely neighboring Li2 sites will be key in the devising of strategies to optimize ionic conductivity in doped LLZO variants. These findings will also aid the investigations of the NMR−structure relations in other energy materials with similar disordered local environments.

■ ASSOCIATED CONTENT

Supporting Information

The Supporting Information is available free of charge at https://pubs.acs.org/doi/10.1021/jacs.9b12685.

Additional experimental ^{17}O, ^{27}Al, and ^{71}Ga NMR spectra and corresponding fitting parameters and powder XRD patterns; technical details for the first-principles calculations; selection of the shifts used for referencing the DFT/GIPAW NMR; benchmark on the DFT settings using the ^{17}O NMR isotropic shieldings; effect of the configurational entropy at finite temperatures; visualization of the simulation models, local coordination analysis, and comparison of computed and experimental NMR spectra; tables comparing the current computed and experimental ^{27}Al and ^{71}Ga NMR parameters to the literature (PDF)

Neighbors within 3.6 Å of oxygen and distances [Å] (XLSX)

https://dx.doi.org/10.1021/jacs.9b12685
J. Am. Chem. Soc. 2020, 142, 3132−3148

AUTHOR INFORMATION

Corresponding Authors

Clare P. Grey − *Department of Chemistry, University of Cambridge, Cambridge CB2 1EW, United Kingdom;* orcid.org/0000-0001-5572-192X; Email: cpg27@cam.ac.uk

Andrew J. Morris − *School of Metallurgy and Materials, University of Birmingham, Birmingham B15 2TT, United Kingdom;* orcid.org/0000-0001-7453-5698; Email: A.J.Morris.1@bham.ac.uk

Authors

Bora Karasulu − *Department of Physics, Cavendish Laboratory, University of Cambridge, Cambridge CB3 0HE, United Kingdom;* orcid.org/0000-0001-8129-8010

Steffen P. Emge − *Department of Chemistry, University of Cambridge, Cambridge CB2 1EW, United Kingdom;* orcid.org/0000-0001-8613-9465

Matthias F. Groh − *Department of Chemistry, University of Cambridge, Cambridge CB2 1EW, United Kingdom;* orcid.org/0000-0002-7436-7177

Complete contact information is available at: https://pubs.acs.org/10.1021/jacs.9b12685

Author Contributions

[‖]B.K. and S.P.E. contributed equally to this work and are the cofirst authors.

Notes

The authors declare no competing financial interest.

ACKNOWLEDGMENTS

Authors would like to acknowledge the funding from the Engineering and Physical Sciences Research Council (EPSRC, Grant EP/P003532/1 for B.K. and M.F.G.), and the German Research Foundation (DFG, Research Fellowship GR 5342/1-1 for M.F.G.). S.P.E. was funded via an EPSRC iCASE (Award 1834544) and via the Royal Society (RP\R1\180147). This work has been performed partly using resources provided by the "Cambridge Service for Data Driven Discovery" (CSD3, http://csd3.cam.ac.uk) system operated by the University of Cambridge Research Computing Service funded by EPSRC Tier-2 capital grant EP/P020259/1. This work also used the resources from the ARCHER UK National Computing Service, funded by the EPSRC (EP/P003532/1). Authors also acknowledge Pedro B. Groszewicz for his extensive support with setting up and analyzing the 3QMAS experiments.

REFERENCES

(1) Murugan, R.; Thangadurai, V.; Weppner, W. Fast Lithium Ion Conduction in Garnet-Type $Li_7La_3Zr_2O_{12}$. *Angew. Chem., Int. Ed.* **2007**, *46* (41), 7778−7781.

(2) Thangadurai, V.; Pinzaru, D.; Narayanan, S.; Baral, A. K. Fast Solid-State Li Ion Conducting Garnet-Type Structure Metal Oxides for Energy Storage. *J. Phys. Chem. Lett.* **2015**, *6* (2), 292−299.

(3) Geiger, C. A.; Alekseev, E.; Lazic, B.; Fisch, M.; Armbruster, T.; Langner, R.; Fechtelkord, M.; Kim, N.; Pettke, T.; Weppner, W. Crystal Chemistry and Stability of "$Li_7La_3Zr_2O_{12}$" Garnet: A Fast Lithium-Ion Conductor. *Inorg. Chem.* **2011**, *50* (3), 1089−1097.

(4) Thangadurai, V.; Narayanan, S.; Pinzaru, D. Garnet-Type Solid-State Fast Li Ion Conductors for Li Batteries: Critical Review. *Chem. Soc. Rev.* **2014**, *43* (13), 4714.

(5) Logéat, A.; Köhler, T.; Eisele, U.; Stiaszny, B.; Harzer, A.; Tovar, M.; Senyshyn, A.; Ehrenberg, H.; Kozinsky, B. From Order to Disorder: The Structure of Lithium-Conducting Garnets $Li_{7-x}La_3Ta_xZr_{2-x}O_{12}$ (x = 0−2). *Solid State Ionics* **2012**, *206*, 33−38.

(6) Wang, Y.; Huq, A.; Lai, W. Insight into Lithium Distribution in Lithium-Stuffed Garnet Oxides through Neutron Diffraction and Atomistic Simulation: $Li_{7-x}La_3Zr_{2-x}Ta_xO_{12}$ (x = 0−2) Series. *Solid State Ionics* **2014**, *255* (230), 39−49.

(7) Chen, Y.; Rangasamy, E.; Liang, C.; An, K. Origin of High Li+ Conduction in Doped $Li_7La_3Zr_2O_{12}$ Garnets. *Chem. Mater.* **2015**, *27* (16), 5491−5494.

(8) Awaka, J.; Kijima, N.; Hayakawa, H.; Akimoto, J. Synthesis and Structure Analysis of Tetragonal $Li_7La_3Zr_2O_{12}$ with the Garnet-Related Type Structure. *J. Solid State Chem.* **2009**, *182* (8), 2046−2052.

(9) Awaka, J.; Takashima, A.; Kataoka, K.; Kijima, N.; Idemoto, Y.; Akimoto, J. Crystal Structure of Fast Lithium-Ion-Conducting Cubic $Li_7La_3Zr_2O_{12}$. *Chem. Lett.* **2011**, *40* (1), 60−62.

(10) Xie, H.; Alonso, J. A.; Li, Y.; Fernández-Díaz, M. T.; Goodenough, J. B. Lithium Distribution in Aluminum-Free Cubic $Li_7La_3Zr_2O_{12}$. *Chem. Mater.* **2011**, *23* (16), 3587−3589.

(11) Xie, H.; Li, Y.; Goodenough, J. B. Low-Temperature Synthesis of $Li_7La_3Zr_2O_{12}$ with Cubic Garnet-Type Structure. *Mater. Res. Bull.* **2012**, *47* (5), 1229−1232.

(12) Kuhn, A.; Narayanan, S.; Spencer, L.; Goward, G.; Thangadurai, V.; Wilkening, M. Li Self-Diffusion in Garnet-Type $Li_7La_3Zr_2O_{12}$ as Probed Directly by Diffusion-Induced ^{7}Li Spin-Lattice Relaxation NMR Spectroscopy. *Phys. Rev. B: Condens. Matter Mater. Phys.* **2011**, *83* (9), 1−11.

(13) Bernstein, N.; Johannes, M. D.; Hoang, K. Origin of the Structural Phase Transition in $Li_7La_3Zr_2O_{12}$. *Phys. Rev. Lett.* **2012**, *109* (20), 1−5.

(14) Inada, R.; Kusakabe, K.; Tanaka, T.; Kudo, S.; Sakurai, Y. Synthesis and Properties of Al-Free $Li_{7-x}La_3Zr_{2-x}Ta_xO_{12}$ garnet Related Oxides. *Solid State Ionics* **2014**, *262*, 568−572.

(15) Uitz, M.; Epp, V.; Bottke, P.; Wilkening, M. Ion Dynamics in Solid Electrolytes for Lithium Batteries: Probing Jump Rates and Activation Energies through Time-Domain Li NMR. *J. Electroceram.* **2017**, *38* (2−4), 142−156.

(16) Pecher, O.; Carretero-Gonzalez, J.; Griffith, K. J.; Grey, C. P. Materials' Methods: NMR in Battery Research. *Chem. Mater.* **2017**, *29* (1), 213−242.

(17) MacKenzie, K. J. D.; Smith, M. E. *Multinuclear Solid-State NMR of Inorganic Materials*; Pergamon: Oxford, U.K., 2002.

(18) Buschmann, H.; Dölle, J.; Berendts, S.; Kuhn, A.; Bottke, P.; Wilkening, M.; Heitjans, P.; Senyshyn, A.; Ehrenberg, H.; Lotnyk, A.; Duppel, V.; Kienle, L.; Janek, J. Structure and Dynamics of the Fast Lithium Ion Conductor "$Li_7La_3Zr_2O_{12}$. *Phys. Chem. Chem. Phys.* **2011**, *13* (43), 19378.

(19) Düvel, A.; Kuhn, A.; Robben, L.; Wilkening, M.; Heitjans, P. Mechanosynthesis of Solid Electrolytes: Preparation, Characterization, and Li Ion Transport Properties of Garnet-Type Al-Doped $Li_7La_3Zr_2O_{12}$ Crystallizing with Cubic Symmetry. *J. Phys. Chem. C* **2012**, *116* (29), 15192−15202.

(20) Hubaud, A. A.; Schroeder, D. J.; Key, B.; Ingram, B. J.; Dogan, F.; Vaughey, J. T. Low Temperature Stabilization of Cubic $(Li_{7-x}Al_{x/3})$-$La_3Zr_2O_{12}$: Role of Aluminum during Formation. *J. Mater. Chem. A* **2013**, *1* (31), 8813−8818.

(21) Wang, D.; Zhong, G.; Dolotko, O.; Li, Y.; McDonald, M. J.; Mi, J.; Fu, R.; Yang, Y. The Synergistic Effects of Al and Te on the Structure and Li^+-Mobility of Garnet-Type Solid Electrolytes. *J. Mater. Chem. A* **2014**, *2* (47), 20271−20279.

(22) Buannic, L.; Orayech, B.; López Del Amo, J.-M.; Carrasco, J.; Katcho, N. A.; Aguesse, F.; Manalastas, W.; Zhang, W.; Kilner, J.; Llordés, A. Dual Substitution Strategy to Enhance Li^+ Ionic Conductivity in $Li_7La_3Zr_2O_{12}$ Solid Electrolyte. *Chem. Mater.* **2017**, *29* (4), 1769−1778.

(23) Rettenwander, D.; Langer, J.; Schmidt, W.; Arrer, C.; Harris, K. J.; Terskikh, V.; Goward, G. R.; Wilkening, M.; Amthauer, G. Site Occupation of Ga and Al in Stabilized Cubic $Li_{7-3(x+y)}Ga_xAl_yLa_3Zr_2O_{12}$ Garnets As Deduced from ^{27}Al and ^{71}Ga MAS NMR at Ultrahigh Magnetic Fields. *Chem. Mater.* **2015**, *27* (8), 3135−3142.

(24) Rettenwander, D.; Blaha, P.; Laskowski, R.; Schwarz, K.; Bottke, P.; Wilkening, M.; Geiger, C. A.; Amthauer, G. DFT Study of the Role of Al^{3+} in the Fast Ion-Conductor $Li_{7-3x}Al^{3+}_xLa_3Zr_2O_{12}$ Garnet. *Chem. Mater.* **2014**, *26* (8), 2617−2623.
(25) Rettenwander, D.; Wagner, R.; Langer, J.; Maier, M. E.; Wilkening, M.; Amthauer, G. Crystal Chemistry of "$Li_7La_3Zr_2O_{12}$" Garnet Doped with Al, Ga, and Fe: A Short Review on Local Structures as Revealed by NMR and Mößbauer Spectroscopy Studies. *Eur. J. Mineral.* **2016**, *28* (3), 619−629.
(26) Howard, M. A.; Clemens, O.; Kendrick, E.; Knight, K. S.; Apperley, D. C.; Anderson, P. A.; Slater, P. R. Effect of Ga Incorporation on the Structure and Li Ion Conductivity of $La_3Zr_2Li_7O_{12}$. *Dalt. Trans.* **2012**, *41* (39), 12048−12053.
(27) Bernuy-Lopez, C.; Manalastas, W.; Lopez del Amo, J. M.; Aguadero, A.; Aguesse, F.; Kilner, J. A. Atmosphere Controlled Processing of Ga-Substituted Garnets for High Li-Ion Conductivity Ceramics. *Chem. Mater.* **2014**, *26* (12), 3610−3617.
(28) Rettenwander, D.; Geiger, C. A.; Tribus, M.; Tropper, P.; Amthauer, G. A Synthesis and Crystal Chemical Study of the Fast Ion Conductor $Li_{7-3x}Ga_xLa_3Zr_2O_{12}$ with x = 0.08 to 0.84. *Inorg. Chem.* **2014**, *53* (12), 6264−6269.
(29) Dervişoğlu, R.; Middlemiss, D. S.; Blanc, F.; Lee, Y. L.; Morgan, D.; Grey, C. P. Joint Experimental and Computational ^{17}O and ^{1}H Solid State NMR Study of $Ba_2In_2O_4(OH)_2$ Structure and Dynamics. *Chem. Mater.* **2015**, *27* (11), 3861−3873.
(30) Middlemiss, D. S.; Blanc, F.; Pickard, C. J.; Grey, C. P. Solid-State NMR Calculations for Metal Oxides and Gallates: Shielding and Quadrupolar Parameters for Perovskites and Related Phases. *J. Magn. Reson.* **2010**, *204* (1), 1−10.
(31) Blanc, F.; Middlemiss, D. S.; Buannic, L.; Palumbo, J. L.; Farnan, I.; Grey, C. P. Thermal Phase Transformations in $LaGaO_3$and $LaAlO_3$ perovskites: An Experimental and Computational Solid-State NMR Study. *Solid State Nucl. Magn. Reson.* **2012**, *42*, 87−97.
(32) Moran, R. F.; Dawson, D. M.; Ashbrook, S. E. Exploiting NMR Spectroscopy for the Study of Disorder in Solids. *Int. Rev. Phys. Chem.* **2017**, *36* (1), 39−115.
(33) Moran, R. F.; Mckay, D.; Tornstrom, P. C.; Aziz, A.; Fernandes, A.; Grau-Crespo, R.; Ashbrook, S. E. Ensemble-Based Modeling of the NMR Spectra of Solid Solutions: Cation Disorder in $Y_2(Sn,Ti)_2O_7$. *J. Am. Chem. Soc.* **2019**, *141* (44), 17838−17846.
(34) McKay, D.; Moran, R. F.; Dawson, D. M.; Griffin, J. M.; Sturniolo, S.; Pickard, C. J.; Berry, A. J.; Ashbrook, S. E. A Picture of Disorder in Hydrous Wadsleyite - Under the Combined Microscope of Solid-State NMR Spectroscopy and Ab Initio Random Structure Searching. *J. Am. Chem. Soc.* **2019**, *141* (7), 3024−3036.
(35) Adams, S.; Rao, R. P. Ion Transport and Phase Transition in $Li_{7-x}La_3(Zr_{2-x}M_x)O_{12}$ (M = Ta^{5+}, Nb^{5+}, x = 0, 0.25). *J. Mater. Chem.* **2012**, *22* (4), 1426−1434.
(36) Miara, L. J.; Ong, S. P.; Mo, Y.; Richards, W. D.; Park, Y.; Lee, J. M.; Lee, H. S.; Ceder, G. Effect of Rb and Ta Doping on the Ionic Conductivity and Stability of the Garnet $Li_{7+2x-y}(La_{3-x}Rb_x)(Zr_{2-y}Ta_y)O_{12}$ ($0 \le x \le 0.375, 0 \le y \le 1$) Superionic Conductor: A First Principles Investigation. *Chem. Mater.* **2013**, *25* (15), 3048−3055.
(37) Zeier, W. G.; Zhou, S.; Lopez-Bermudez, B.; Page, K.; Melot, B. C. Dependence of the Li-Ion Conductivity and Activation Energies on the Crystal Structure and Ionic Radii in $Li_6MLa_2Ta_2O_{12}$. *ACS Appl. Mater. Interfaces* **2014**, *6* (14), 10900−10907.
(38) Jalem, R.; Rushton, M. J. D. J. D.; Manalastas, W.; Nakayama, M.; Kasuga, T.; Kilner, J. A.; Grimes, R. W. Effects of Gallium Doping in Garnet-Type $Li_7La_3Zr_2O_{12}$ Solid Electrolytes. *Chem. Mater.* **2015**, *27* (8), 2821−2831.
(39) Yeandel, S.; Chapman, B. J.; Slater, P. R.; Goddard, P. Structure and Lithium Ion Dynamics in Fluoride Doped Cubic LLZO ($Li_7La_3Zr_2O_{12}$) Garnet for Li Solid State Battery Applications. *J. Phys. Chem. C* **2018**, *122*, 27811.
(40) García Daza, F. A.; Bonilla, M. R.; Llordés, A.; Carrasco, J.; Akhmatskaya, E. Atomistic Insight into Ion Transport and Conductivity in Ga/Al-Substituted $Li_7La_3Zr_2O_{12}$ Solid Electrolytes. *ACS Appl. Mater. Interfaces* **2019**, *11* (1), 753−765.
(41) Miara, L. J.; Richards, W. D.; Wang, Y. E.; Ceder, G. First-Principles Studies on Cation Dopants and Electrolyte|Cathode Interphases for Lithium Garnets. *Chem. Mater.* **2015**, *27* (11), 4040−4047.
(42) Meier, K.; Laino, T.; Curioni, A. Solid-State Electrolytes: Revealing the Mechanisms of Li-Ion Conduction in Tetragonal and Cubic LLZO by First-Principles Calculations. *J. Phys. Chem. C* **2014**, *118* (13), 6668−6679.
(43) Rettenwander, D.; Redhammer, G.; Preishuber-Pflügl, F.; Cheng, L.; Miara, L.; Wagner, R.; Welzl, A.; Suard, E.; Doeff, M. M.; Wilkening, M.; Fleig, J.; Amthauer, G. Structural and Electrochemical Consequences of Al and Ga Cosubstitution in $Li_7La_3Zr_2O_{12}$ Solid Electrolytes. *Chem. Mater.* **2016**, *28* (7), 2384−2392.
(44) Canepa, P.; Dawson, J. A.; Sai Gautam, G.; Statham, J. M.; Parker, S. C.; Islam, M. S. Particle Morphology and Lithium Segregation to Surfaces of the $Li_7La_3Zr_2O_{12}$ Solid Electrolyte. *Chem. Mater.* **2018**, *30* (9), 3019−3027.
(45) Xu, M.; Park, M. S.; Lee, J. M.; Kim, T. Y.; Park, Y. S.; Ma, E. Mechanisms of Li^+ Transport in Garnet-Type Cubic $Li_{3+x}La_3M_2O_{12}$ (M = Te, Nb, Zr). *Phys. Rev. B: Condens. Matter Mater. Phys.* **2012**, *85* (5), 1−5.
(46) Nakayama, M.; Kotobuki, M.; Munakata, H.; Nogami, M.; Kanamura, K. First-Principles Density Functional Calculation of Electrochemical Stability of Fast Li Ion Conducting Garnet-Type Oxides. *Phys. Chem. Chem. Phys.* **2012**, *14* (28), 10008−10014.
(47) Clark, S. J.; Segall, M. D.; Pickard, C. J.; Hasnip, P. J.; Probert, M. J.; Refson, K.; Payne, M. C. First Principles Methods Using {CASTEP}. *Z. Kristallogr. - Cryst. Mater.* **2005**, *220*, 567−570.
(48) Segall, M. D.; Lindan, P. J. D.; Probert, M. J.; Pickard, C. J.; Hasnip, P. J.; Clark, S. J.; Payne, M. C. First-Principles Simulation: Ideas, Illustrations and the CASTEP Code. *J. Phys.: Condens. Matter* **2002**, *14* (11), 2717−2744.
(49) Perdew, J. P.; Burke, K.; Ernzerhof, M. Generalized Gradient Approximation Made Simple. *Phys. Rev. Lett.* **1996**, *77* (18), 3865−3868.
(50) Monkhorst, H. J.; Pack, J. D. Special Points for Brillouin-Zone Integrations. *Phys. Rev. B* **1976**, *13* (12), 5188−5192.
(51) Liu, D. C.; Nocedal, J. On the Limited Memory BFGS Method for Large Scale Optimization. *Math. Program.* **1989**, *45* (1−3), 503−528.
(52) Nocedal, J. Updating Quasi-Newton Matrices with Limited Storage. *Math. Comput.* **1980**, *35* (151), 773−773.
(53) Pickard, C. J.; Mauri, F. All-Electron Magnetic Response with Pseudopotentials: NMR Chemical Shifts. *Phys. Rev. B: Condens. Matter Mater. Phys.* **2001**, *63* (24), 245101.
(54) Yates, J. R.; Pickard, C. J.; Mauri, F. Calculation of NMR Chemical Shifts for Extended Systems Using Ultrasoft Pseudopotentials. *Phys. Rev. B: Condens. Matter Mater. Phys.* **2007**, *76* (2), 1−11.
(55) Profeta, M.; Mauri, F.; Pickard, C. J. Accurate First Principles Prediction of ^{17}O NMR Parameters in SiO_2: Assignment of the Zeolite Ferrierite Spectrum. *J. Am. Chem. Soc.* **2003**, *125* (2), 541−548.
(56) Sturniolo, S. SOPRANO—A Library to Crack Crystals. SOPRANO—A library to crack crystals. https://ccpforge.cse.rl.ac.uk/gf/project/soprano/.
(57) Hoppe, R. Effective Coordination Numbers (ECoN) and Mean Active Fictive Ionic Radii (MEFIR) [1,2]*. *Zeitschrift für Krist.* **1979**, *150* (1−4), 23−52.
(58) Baur, W. H. The Geometry of Polyhedral Distortions. Predictive Relationships for the Phosphate Group. *Acta Crystallogr., Sect. B: Struct. Crystallogr. Cryst. Chem.* **1974**, *30* (5), 1195−1215.
(59) Robinson, K.; Gibbs, G. V.; Ribbe, P. H. Quadratic Elongation: A Quantitative Measure of Distortion in Coordination Polyhedra. *Science (Washington, DC, U. S.)* **1971**, *172* (3983), 567−570.
(60) Fleet, M. E. Distortion Parameters for Coordination Polyhedra. *Mineral. Mag.* **1976**, *40*, 531−533.
(61) Brese, N. E.; O'Keeffe, M. IUCr. Bond-Valence Parameters for Solids. *Acta Crystallogr., Sect. B: Struct. Sci.* **1991**, *47* (2), 192−197.

https://dx.doi.org/10.1021/jacs.9b12685
J. Am. Chem. Soc. 2020, 142, 3132−3148

(62) Brown, I. D.; Altermatt, D. IUCr. Bond-Valence Parameters Obtained from a Systematic Analysis of the Inorganic Crystal Structure Database. *Acta Crystallogr., Sect. B: Struct. Sci.* **1985**, *41* (4), 244−247.
(63) Momma, K.; Izumi, F. VESTA: A Three-Dimensional Visualization System for Electronic and Structural Analysis. *J. Appl. Crystallogr.* **2008**, *41* (3), 653−658.
(64) Li, Y.; Han, J.-T.; Wang, C.-A.; Xie, H.; Goodenough, J. B. Optimizing Li^+ Conductivity in a Garnet Framework. *J. Mater. Chem.* **2012**, *22* (30), 15357.
(65) Yang, S.; Shore, J.; Oldfield, E. Oxygen-17 Nuclear Magnetic Resonance Spectroscopic Study of the Lanthanide Oxides. *J. Magn. Reson.* **1992**, *99* (2), 408−412.
(66) Bastow, T. J.; Stuart, S. N. ^{17}O NMR in Simple Oxides. *Chem. Phys.* **1990**, *143* (3), 459−467.
(67) Ash, J. T.; Grandinetti, P. J. Solid-State NMR Characterization of ^{69}Ga and ^{71}Ga in Crystalline Solids. *Magn. Reson. Chem.* **2006**, *44* (9), 823−831.
(68) Chan, J. C. C.; Eckert, H. High-Resolution $^{27}Al-^{19}F$ Solid-State Double Resonance NMR Studies of $AlF_3-BaF_2-CaF_2$ Glasses. *J. Non-Cryst. Solids* **2001**, *284* (1), 16−21.
(69) *Topspin v3.5, Software for NMR Spectral Analysis*; Bruker Biospin: Rheinstetten, Germany, 2018.
(70) Massiot, D.; Fayon, F.; Capron, M.; King, I.; Le Calvé, S.; Alonso, B.; Durand, J. O.; Bujoli, B.; Gan, Z.; Hoatson, G. Modelling One- and Two-Dimensional Solid-State NMR Spectra. *Magn. Reson. Chem.* **2002**, *40* (1), 70−76.
(71) Haouas, M.; Taulelle, F.; Martineau, C. Recent Advances in Application of ^{27}Al NMR Spectroscopy to Materials Science. *Prog. Nucl. Magn. Reson. Spectrosc.* **2016**, *94*−*95*, 11−36.
(72) Florian, P.; Gervais, M.; Douy, A.; Massiot, D.; Coutures, J.-P. A Multi-Nuclear Multiple-Field Nuclear Magnetic Resonance Study of the $Y_2O_3-Al_2O_3$ Phase Diagram. *J. Phys. Chem. B* **2001**, *105* (2), 379−391.
(73) Skibsted, J.; Henderson, E.; Jakobsen, H. J. Characterization of Calcium Aluminate Phases in Cements by Aluminum-27 MAS NMR Spectroscopy. *Inorg. Chem.* **1993**, *32* (6), 1013−1027.
(74) Matsuda, Y.; Sakamoto, K.; Matsui, M.; Yamamoto, O.; Takeda, Y.; Imanishi, N. Phase Formation of a Garnet-Type Lithium-Ion Conductor $Li_{7-3x}Al_xLa_3Zr_2O_{12}$. *Solid State Ionics* **2015**, *277*, 23−29.
(75) Rangasamy, E.; Wolfenstine, J.; Sakamoto, J. The Role of Al and Li Concentration on the Formation of Cubic Garnet Solid Electrolyte of Nominal Composition $Li_7La_3Zr_2O_{12}$. *Solid State Ionics* **2012**, *206*, 28−32.
(76) Massiot, D.; Farnan, I.; Gautier, N.; Trumeau, D.; Trokiner, A.; Coutures, J. P. ^{71}Ga and ^{69}Ga Nuclear Magnetic Resonance Study of β-Ga_2O_3: Resolution of Four- and Six-Fold Coordinated Ga Sites in Static Conditions. *Solid State Nucl. Magn. Reson.* **1995**, *4* (4), 241−248.
(77) Massiot, D.; Vosegaard, T.; Magneron, N.; Trumeau, D.; Montouillout, V.; Berthet, P.; Loiseau, T.; Bujoli, B. ^{71}Ga NMR of Reference Ga_{IV}, Ga_V, and Ga_{VI} Compounds by MAS and QPASS, Extension of Gallium/Aluminum NMR Parameter Correlation. *Solid State Nucl. Magn. Reson.* **1999**, *15* (3), 159−169.
(78) Kubicek, M.; Wachter-Welzl, A.; Rettenwander, D.; Wagner, R.; Berendts, S.; Uecker, R.; Amthauer, G.; Hutter, H.; Fleig, J. Oxygen Vacancies in Fast Lithium-Ion Conducting Garnets. *Chem. Mater.* **2017**, *29* (17), 7189−7196.
(79) Seymour, I. D.; Middlemiss, D. S.; Halat, D. M.; Trease, N. M.; Pell, A. J.; Grey, C. P. Characterizing Oxygen Local Environments in Paramagnetic Battery Materials via ^{17}O NMR and DFT Calculations. *J. Am. Chem. Soc.* **2016**, *138* (30), 9405−9408.
(80) Hope, M. A.; Halat, D. M.; Lee, J.; Grey, C. P. A ^{17}O Paramagnetic NMR Study of Sm_2O_3, Eu_2O_3, and Sm/Eu-Substituted CeO_2. *Solid State Nucl. Magn. Reson.* **2019**, *102*, 21−30.
(81) Martel, L.; Naji, M.; Popa, K.; Vigier, J.-F.; Somers, J. Fingerprint of Local Disorder in Long Range Ordered Isometric Pyrochlores. *Sci. Rep.* **2017**, *7* (1), 12269.
(82) Ali, F.; Smith, M. E.; Steuernagel, S.; Whitfield, H. J. ^{17}O Solid-State NMR Examination of La_2O_3 Formation. *J. Mater. Chem.* **1996**, *6* (2), 261.
(83) Bastow, T. J.; Dirken, P. J.; Smith, M. E.; Whitfield, H. J. Factors Controlling the ^{17}O NMR Chemical Shift in Ionic Mixed Metal Oxides. *J. Phys. Chem.* **1996**, *100* (47), 18539−18545.
(84) Buannic, L.; Blanc, F.; Hung, I.; Gan, Z.; Grey, C. P. Probing the Local Structures and Protonic Conduction Pathways in Scandium Substituted $BaZrO_3$ by Multinuclear Solid-State NMR Spectroscopy. *J. Mater. Chem.* **2010**, *20* (30), 6322.
(85) Kim, N.; Grey, C. P. 17O MAS NMR Study of the Oxygen Local Environments in the Anionic Conductors $Y_2(B_{1-x}B'_x)_2O_7$(B, B′=Sn, Ti, Zr). *J. Solid State Chem.* **2003**, *175* (1), 110−115.
(86) Allen, J. L.; Wolfenstine, J.; Rangasamy, E.; Sakamoto, J. Effect of Substitution (Ta, Al, Ga) on the Conductivity of $Li_7La_3Zr_2O_{12}$. *J. Power Sources* **2012**, *206*, 315−319.
(87) Ong, S. P.; Mo, Y.; Richards, W. D.; Miara, L.; Lee, H. S.; Ceder, G. Phase Stability, Electrochemical Stability and Ionic Conductivity of the $Li_{10\pm1}MP_2X_{12}$ (M = Ge, Si, Sn, Al or P, and X = O, S or Se) Family of Superionic Conductors. *Energy Environ. Sci.* **2013**, *6* (1), 148−156.
(88) Wagner, R.; Rettenwander, D.; Redhammer, G. J.; Tippelt, G.; Sabathi, G.; Musso, M. E.; Stanje, B.; Wilkening, M.; Suard, E.; Amthauer, G. Synthesis, Crystal Structure, and Stability of Cubic $Li_{7-x}La_3Zr_{2-x}Bi_xO_{12}$. *Inorg. Chem.* **2016**, *55* (23), 12211−12219.
(89) Grau-Crespo, R.; Hamad, S.; Catlow, C. R. A.; De Leeuw, N. H. Symmetry-Adapted Configurational Modelling of Fractional Site Occupancy in Solids. *J. Phys.: Condens. Matter* **2007**, *19* (25), 256201.
(90) Pimentel, H. R. X.; Aguiar, D. L. M.; San Gil, R. A. S.; Souza, E. F.; Ferreira, A. R.; Leitão, A. A.; Alencastro, R. B.; Menezes, S. M. C.; Chiaro, S. S. X. ^{17}O MAS NMR and First Principles Calculations of ZrO_2 Polymorphs. *Chem. Phys. Lett.* **2013**, *555*, 96−100.
(91) Wenger, M.; Armbruster, T. Crystal Chemistry of Lithium: Oxygen Coordination and Bonding. *Eur. J. Mineral.* **1991**, *3* (2), 387−400.
(92) Maurer, M. Electric Field Gradients of Randomly Disordered Compounds. *Phys. Rev. B: Condens. Matter Mater. Phys.* **1986**, *34* (12), 8996−8999.
(93) Czjzek, G. Distribution of Nuclear Quadrupole Splittings in Amorphous Materials and the Topology of the (V_{ZZ}, η)-Parameter Space. *Hyperfine Interact.* **1983**, *14* (3), 189−194.
(94) Neuville, D. R.; Cormier, L.; Massiot, D. Al Environment in Tectosilicate and Peraluminous Glasses: A ^{27}Al MQ-MAS NMR, Raman, and XANES Investigation. *Geochim. Cosmochim. Acta* **2004**, *68* (24), 5071−5079.
(95) d'Espinose de Lacaillerie, J.-B.; Fretigny, C.; Massiot, D. MAS NMR Spectra of Quadrupolar Nuclei in Disordered Solids: The Czjzek Model. *J. Magn. Reson.* **2008**, *192* (2), 244−251.
(96) Car, G. Le; Bureau, B.; Massiot, D. An Extension of the Czjzek Model for the Distributions of Electric Field Gradients in Disordered Solids and an Application to NMR Spectra of ^{71}Ga in Chalcogenide Glasses. *J. Phys.: Condens. Matter* **2010**, *22* (6), 065402.
(97) Seleznyova, K.; Sergeev, N. A.; Olszewski, M.; Stępień, P.; Yagupov, S. V.; Strugatsky, M. B.; Kliava, J. Fitting MAS NMR Spectra in Crystals with Local Disorder: Czjzek's vs. Maurer's Model for ^{11}B and ^{71}Ga in Polycrystalline Gallium Borate. *Solid State Nucl. Magn. Reson.* **2017**, *85*−*86*, 12−18.
(98) Wu, J.-F.; Chen, E.-Y.; Yu, Y.; Liu, L.; Wu, Y.; Pang, W. K.; Peterson, V. K.; Guo, X. Gallium-Doped $Li_7La_3Zr_2O_{12}$ Garnet-Type Electrolytes with High Lithium-Ion Conductivity. *ACS Appl. Mater. Interfaces* **2017**, *9* (2), 1542−1552.
(99) Wagner, R.; Redhammer, G. J.; Rettenwander, D.; Senyshyn, A.; Schmidt, W.; Wilkening, M.; Amthauer, G. Crystal Structure of Garnet-Related Li-Ion Conductor $Li_{7-3x}Ga_xLa_3Zr_2O_{12}$: Fast Li-Ion Conduction Caused by a Different Cubic Modification? *Chem. Mater.* **2016**, *28* (6), 1861−1871.
(100) Bottke, P.; Rettenwander, D.; Schmidt, W.; Amthauer, G.; Wilkening, M. Ion Dynamics in Solid Electrolytes: NMR Reveals the Elementary Steps of Li^+ Hopping in the Garnet $Li_{6.5}La_3Zr_{1.75}Mo_{0.25}O_{12}$. *Chem. Mater.* **2015**, *27* (19), 6571−6582.

https://dx.doi.org/10.1021/jacs.9b12685
J. Am. Chem. Soc. 2020, 142, 3132−3148